Master's Thesis, 30 ECTS

Elastic hyperspectral lidar for detecting coherent backscatter from insects

Division of Combustion Physics
Department of Physics
Faculty of Engineering LTH
Lund University

LUNDS UNIVERSITET

Author:
Lauro Müller

Supervisor:
Mikkel Brydegaard
Co-supervisor:
Hampus Månefjord

June 2022

Populärvetenskaplig sammanfattning

Fjärranalys av insekter med laserljus

I detta examensarbete utvecklades ett instrument som använder en bredbandig ljusstråle för fjärranalys av insekter. Tjockleken av en jungfrusländas vinge mättes på 87 m *avstånd och med en* 4 nm *noggrannhet.*

Insekter spelar en huvudroll i ekosystemet och är avgörande för den biologiska mångfalden. Att urskilja och övervaka var miljontals insekter i våra miljöer befinner sig är en stor utmaning. Användning av laser och modern fotonik gör det möjligt att upptäcka insekter i stora mängder på distans utan att fånga dem. Antalet insekter har minskat drastiskt under de senaste årtiondena. Lasermätningar kan ge nya insikter om vilka åtgärder som måste vidtas för att rädda insekterna.

En lidar (laser radar) är ett optiskt instrument som använder laserljus för att mäta vart i landskapet olika objekt befinner sig. Laserljuset färdas från lidarn till objektet där det studsar tillbaka och samlas in av lidarn. Vanligtvis bestäms avståndet genom att mäta tiden ljuset tar att färdas från lidarn till objektet och tillbaka. I en Scheimpflug lidar, å andra sidan, mäts avståndet i stället med triangulering. Det innebär att ljuset som reflekteras från olika avstånd avbildas, med hjälp av optik i en specifik konfiguration, på olika delar av en kamerasensor.

I detta examensarbete utvecklades en hyperspektral Scheimpflug lidar som testades för insektmätningar. Lidarn ställdes på ett fält medan strålen från lidarenheten lyste över fältet. Insekter som flög genom strålen reflekterade en del av ljuset, vilket upptäcktes med lidarn. Förutom avstånd, kan en hyperspektral lidar också mäta ljusspektrumet från bakspridningen över stora avstånd. När bredbandigt ljus träffar ett föremål, kan vissa våglängder vara i resonans med molekylära absorptionsband eller nanostrukturer, varvid skillnader uppstår i spektrumet. Ett spektrum visar vilka våglängder målet reflekterar och kan fungera som ett fingeravtryck för olika arter. Ljuset som träffar ett tunt lager av ett genomskinligt material kan uppvisa en effekt som heter tunnfilmsinterferens. Denna effekt ligger bakom till exempel regnbågefärgerna i såpbubblor eller färgen på halsen av en duva. Effekten uppstår från reflektioner från lagrets över- och undersidor som sammanfaller och gör att vissa våglängder tar ut varandra medan andra våglängder förstärker varandra. Ett så kallat tunnfilmsinterferensspektrum kan sedan användas för att beräkna tjockleken av lagret.

För att testa lidarn som utvecklades, mättes spektrumet av en jungfrusländas vinge på 87 m avstånd. När ljuset träffade vingen fungerade den som ett tunt lager och orsakade därmed tunnfilminterferens. Spektrumet som mättes var alltså ett interferensspektrum som kunde användas för att beräkna vingens tjocklek. Mätningen tog 4 ms och den resulterande tjockleken är $1.417\,\mu\text{m} \pm 4\,\text{nm}$, vilket är en anmärkningsvärt hög noggrannhet och dessa resultat kan föra fjärrövervakningen av insekter till en ny nivå.

Abstract

Insects play a major role in the ecosystem and are an important factor for biodiversity. Using laser remote sensing to distinguish and monitor the millions of insects *in-situ*, holds large potential to speed up and improve the otherwise time consuming process of trapping and subsequent analysis. In this work, the spectral analyser for an elastic hyper spectral lidar in the SWIR, with 64 effective spectral bands was developed, to monitor the aerofauna. The spectral analyser was designed using raytracing, CAD-desing and 3D-printing. As a proof of principle, the lidar was tested during a field campaign where the coherent backscatter of a damselfly was measured at a distance of 87 m without averaging (4 ms exposure time). From the backscattered signal, a thin-film interference pattern could be retrieved, from which the wing membrane thickness could be determined to 1417 nm with a precision of $\pm$ 4 nm. This result is very promising for future entomological studies and can bring species specificity of remote sensing of insects to a new level. Further applications of this lidar can be monitoring of gases, particles in the atmosphere and also vegetation structure.

Acknowledgements

I would like to express my graduate to the following people for their contribution to this project.

To Mikkel Brydegaard, who supervised me and made this thesis possible. For all the help and inputs you gave me throughout this thesis. I felt privileged to be part of your research group and work on a interesting project that ranged from lab work to field campaigns.

To Hampus Månefjord, for co-supervising me and giving me a lot of helpful advice. Especially for sharing your construction and 3D-printing skills and also for being an excellent beach volleyball partner.

To Meng Li, for providing the reference measurements of the damselfly and always helping me at any time, even on Sunday evenings during my trips to Nyteboda.

To Jacobo Salvador, who built the first prototype of the spectral analyser.

To Anna Brandt, for being my office buddy and opponent and for helping me with my e-mails.

To all my colleagues at combustion physics. I appreciated very much the welcoming atmosphere at the department.

To Daniel Díaz and Andrea Angella, for the fundamental discussions.

To Jadranka Rota, for providing the museum specimen which were used during the field measurements.

To Julio Hernandez, for providing the hyperspectral camera setup which was used for the reference measurement.

To Nina Reistad, for providing the supercontiuum light source.

To Anna Runemark and Carsten Kirkeby, for the support during the field campaign.

To Adrian Roth, for the technical support during the presentation.

To the European Research Council ERC, for funding the InGaAs camera and other equipment.

Contents

1 Introduction

1.1 Motivation

An intact biosphere is essential to provide the necessary conditions for life on this planet. Optical remote sensing is an important technique for monitoring the biosphere [1],[2]. It allows non-destructive, species sensitive sensing of vast areas. Typical specimen which are to be monitored are for instance gases [3], aerosols [4],[5], waterbodies [6], vegetation [7] and areofauna [8]. In this work, the main focus will be placed in developing a hyperspectral lidar to monitor the aerofauna where insects play a major role. The diversity and abundance of insects has declined drastically in the recent years [9],[10]. Insects are essential in an ecosystem and an important factor for biodiversity.
Lidar can be exploited [8] for remote sensing the biosphere where the backscattered light of atmospheric constituents is detected.
As opposed to previous lidar with only one color band, dual-band lidar have been demonstrated for the study of insects [11] and atmospheric particles [4]. Hyperspectral lidar have an increased number of spectral bands which allows retrieving the spectrum of the target.
Knowing the spectrum of an object is crucial for target classification. A higher number of spectral bands will enhance the specificity. In order to create a tool to monitor the aerofauna, a Scheimpflug hyperspectral lidar in the short wave infrared (SWIR) [5],[3], with an increased amount of spectral bands is to be developed.
It has been shown in previous studies [12], [13], [14] that structural colors such as thin film interference occur in insect wings and that these thin-film interference fringes of insect wings, can be exploited to deduced the wing thickness. Thus, being able to measure the fringes with a hyperspectral lidar would be relevant for insect classification as the wing thickness varies with species and sex.

Another application can be the study of surface roughness of moth wings. In the SWIR, the amount of specular reflection on a moth wing increases with wavelength [15],[16].
Surface roughness is an important tool for the identification of night-flying moth [17] (in print).

Further applications of this hyperspectral lidar can be continuous-wave differential absorption lidar [18] for the study of gases, particles in the atmosphere [19] and vegetation.

1.2 State of the art

In conventional lidar [1], diode pumped solid state lasers (DPSS) are utilized where the time-of-flight (ToF) is used to infer range.
Applying ToF in hyperspectral lidar, however, limits the system in range drastically, as broadband light sources are often used to deduce the spectrum. These supercontiuum fiber lasers (see chapter 3.2) exhibit significantly lower peak powers than DPSS. Supercontinuum lasers also work at a notably higher repetition rate which limits the ambiguous range.
In [20] a ToF hyperspectral lidar with 8 effective spectral bands and a range up to 20 m is presented for remote sensing of vegetation.

In [21] another ToF-lidar with 8 spectral bands was developed for the purpose of rock classification in mines with a range of roughly 30 m.

The Scheimpflug lidar method [22] on the other hand, acquires range resolution by triangulation. As opposed to ToF-lidar, this method is not limited by a maximum ambiguous range and can thus be applied for short range applicatons such as in combustion diagnostics [23] as well as in long range applications where atmospheric particles are measured [24].

A hyperspectral lidar can be classified in elastic and inelastic-lidar. When detecting the elastic backscatter, a broadband light source can be used to receive spectral information. With supercontinuum laser technology it is possible to achieve laser light with a spectral range of $480\,\text{nm} - 2400\,\text{nm}$. Hyperspectral lidar based on supercontinuum lasers can be used for different applications such as to study vegetation [20],[25],[26] and for rock classification [21].
In inelastic lidar applications, narrowband laser light can be used to excite certain molecules from which the laser induced fluorescence (LIF) is measured. LIF can be applied in lidar systems for vegetation monitoring where the fluorescence of chlorophyll is measured [7]. Other promising applications are the monitoring of powder-tagged insects where the fluorescence of an applied powder is measured [27] or detecting the position and behaviour of aquatic organism [28].

1.3 Outline and aim

In this work, a Scheimpflug hyperspectral lidar in the short wave infrared (SWIR) i.e. $1000\,\text{nm} - 1600\,\text{nm}$, was developed, assembled, characterised and tested. As a first step, a previously developed prototype was characterised. Several issues that appeared in the characterisation made it necessary to redesign the system. The redesign, which was the main part of this work included raytracing with Zemax, designing the opto-mechanical setup with CAD as well as 3D-printing, assembling and alignment of the system. Moreover, the new system was characterised in a similar manner as the first prototype to compare them and make sure that the mentioned issues no longer appear. In order to test the system, field measurements at Stensoffas field station in Revingehed, Sweden were carried out where different specimen such as insect wings were measured.
As a last step, the recorded data was analysed in Matlab where a thin film fringe of a damselfly could be retrieved from which the wing thickness could be calculated.

2 Light-tissue interaction

This section gives a brief overview of scattering and radiation processes to understand the significance of specular reflections which will be observed when investigating the reflectance of a damselfly wing. A detailed description of the different radiation and scattering mechanisms is found in [2],[29],[30],[31] and [32].

2.1 Scattering

Light impinging on a sample can be scattered in different ways. The scattering process can be coherent or incoherent. Coherent scattered light 'remembers' phase, polarization and propagation direction of the incident light.

Specular elastic reflection is an example of coherent scattering and happens at the boundary between two media with different refractive indices. The magnitude of the reflection is governed by the Fresnel equations and depends on the refractive index difference of the interface. As specular reflections are not directly influenced by molecular absorption, the reflection does not contain the spectral imprint of the sample. The direction of the reflection depends on the incident angle and surface normal orientation. For instance, when a collimated laser beam is impinging on a specular target, the collimation can be partly conserved and result in a back propagating laser beam. The specular reflected light is furthermore termed co-polarised as the polarization of the incident light is retained. A fraction of the light will also enter the medium and be refracted according to Snell's law. In a non-turbid medium, the entered light will exit the medium without being scattered which is referred to as ballistic photons.

Diffuse elastic reflection on the other hand, is an example of incoherent scattering. The light penetrates the sample, is multiple scattered before exiting the sample again after a certain migration distance. A highly scattering medium results in a short migration distance and shallow penetration depth. The multiple scattered photons loose information about phase and polarization of the incident light. The reflection is thus incoherent and depolarized. The diffuse reflection, however, contains spectral information of the sample as part of the spectrum is absorbed. A schematic illustration of specular and diffuse reflections is depicted in figure 1.

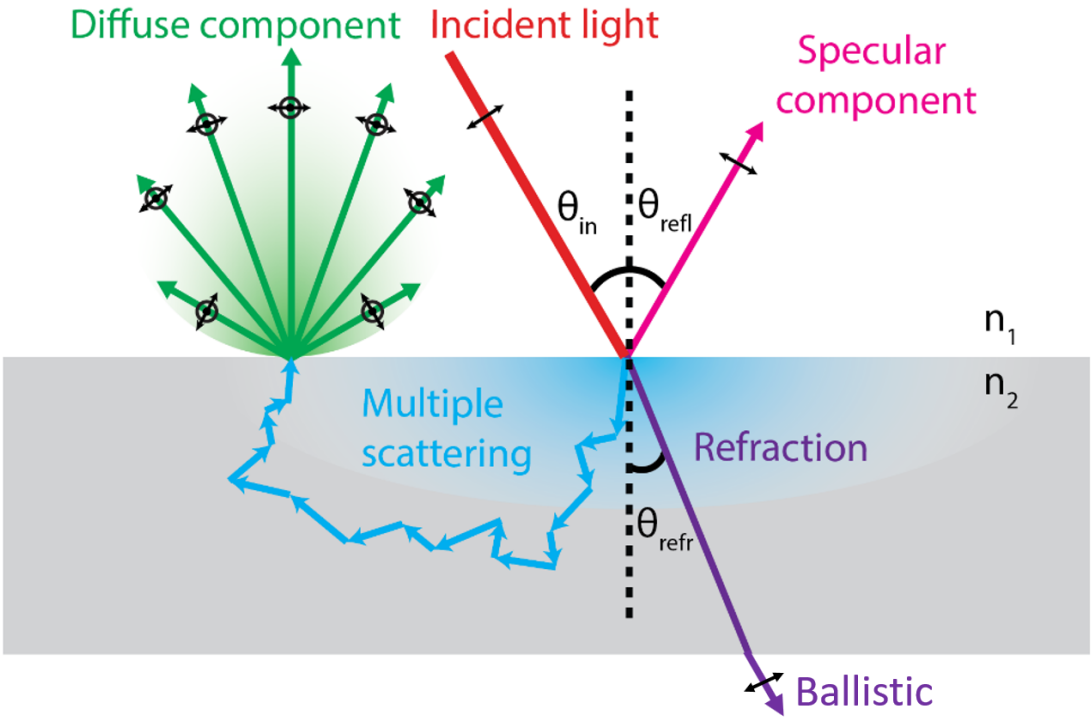

Figure 1: Schematic illustration of specular and diffuse reflections. The specular reflection is reflected at the surface with the same angle as the incidence angle while the diffuse reflection enters the medium, is multiple scattered, and exits the medium in a diffuse manner. Photons that are transmitted without being scattered are referred to as ballistic photons. Figure adapted from [31].

In elastic scattering which was discussed so far, the photon energy is conserved during the scattering process. In inelastic scattering on the other hand, the energy of the scattered photons is different compared to the incoming photons.
An example of inelastic scattering is spontaneous Raman scattering. Raman can either be red-shifted (Stoke) or blue-shifted (anti-Stoke).
Figure 2 a) shows the schematic energy level diagram for Rayleigh (elastic) and Raman (inelastic) scattering with the corresponding spectrum in panel b).

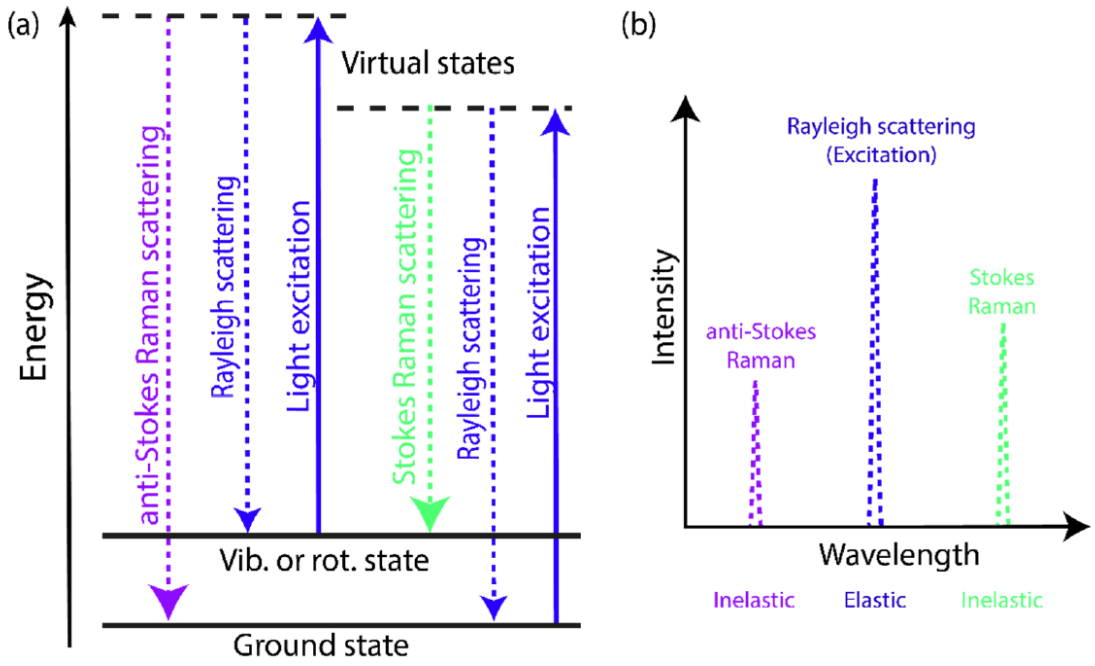

Figure 2: Energy level diagram for Rayleigh and Raman scattering a), with the corresponding spectrum b). Figure from [31].

When a photon is scattered on a single particle, the direction it can take is described by statistical scattering phase functions and depends on wavelength, particle size and particle shape. The different scattering phase functions are derived and discussed in detail in the chapter Scattering in [32].

2.2 Thin-film interference

Thin-film interference occurs from boundary reflections at a Fabry-Pérot etalon. In figure 3 a chitin membrane surrounded by air presents an example of such a thin-film structure. When broadband light is impinging on the etalon, the partial reflections from the first and second boundary interfere. If the phase difference between the two reflections is a multiple of $\lambda/2$, they will interfere destructively and in case the phase difference is a multiple of λ, they will interfere constructively. Moreover, a phase-flip occurs at the interface from air to chitin since $n_{\text{air}} < n_{\text{chitin}}$, which also contributes to the phase difference. For a thin-film membrane surrounded by a medium with a lower refractive index, for instance air-chitin-air, and an incident angle $\theta = 0\,^{\circ}$, constructive interference λ_{max} is obtained at,

$$\lambda_{\text{max}} = \frac{2nd}{m - \frac{1}{2}}, \tag{1}$$

where d is the membrane thickness, n the refractive index of the membrane and m belongs to positive, natural integer numbers.

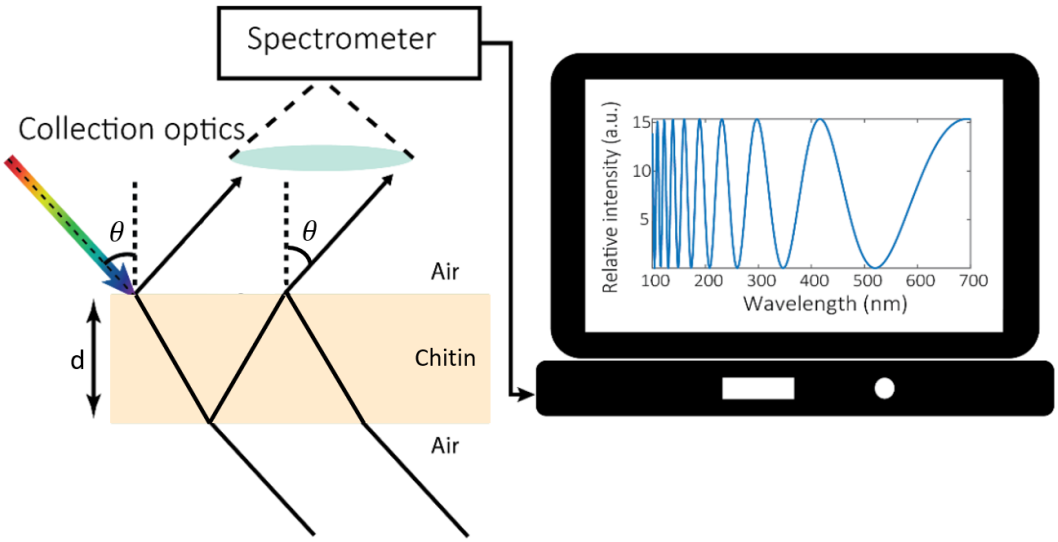

Figure 3: Thin-film interference from a chitin membrane approximated as a Fabry-Pérot etalon. The reflections from the air-chitin boundaries interfere destructively and constructively causing an interference pattern with increasing periodicity for longer wavelengths. Figure adapted from [31]

Each peak in the interference pattern is termed spectral fringe. The separation of the fringes depends on wavelength λ, the thickness of the membrane d and the angle of incidence θ. The total reflectance from a thin-film reflector furthermore depends on the Fresnel equations which takes into account state of polarisation, incidence angle and refractive index n. The analytical model for the total reflectance R_{thinfilm} of a thin film membrane is described by [33] and shown in equation 2.

$$R_{\text{thinfilm}} = \frac{4R_{\text{Fresnel}}^2 \sin^2(2\pi d\sqrt{n_{\text{chitin}}^2 - \sin^2\theta}/\lambda)}{(1 - R_{\text{Fresnel}}^2)^2 + 4R_{\text{Fresnel}}^2 \sin^2(2\pi d\sqrt{n_{\text{chitin}}^2 - \sin^2\theta}/\lambda)} \tag{2}$$

The wavelength dependant refractive index of chitin is $n_{\text{chitin}} = A + B/\lambda^2$ with $A = 1.517$ and $B = 8800\,\text{nm}^2$. The refractive index of air is assumed to be $n_{\text{air}} = 1$. R_{Fresnel} is the reflectance from the Fresnel equations. In lidar, the backscattered light is collected when the incident angle $\theta = 0\,^\circ$, which results in a simplified expression, $R_{\text{Fresnel}} = \dfrac{n_{\text{air}} - n_{\text{chitin}}}{n_{\text{air}} + n_{\text{chitin}}}$, for both states of polarisation.
Colors that are not caused by pigment absorption but through inferences are termed structural colors. In the further course of this thesis, the thin-film interference of a damselfly wing is measured, hence the example of chitin in figure 3.

2.3 Fluorescence

When light is impinging on a fluorescent sample, which applies to almost all biological samples, the light can also be absorbed and remitted as fluorescence. The incident light has

to match a real energy transition of the molecule in order to be absorbed. This is unlike Raman scattering which is a non-resonant process e.g. the excitation happens to a virtual level and thus the emission is instantaneous [31]. The fluorescent emission tends to be stoke shifted as the photons loose part of their energy through non-radiatively relaxation. Figure 4 shows the schematic energy level diagram for absorption and fluorescent emission with the corresponding spectrum. The energy diagram is depicted for gases a) where the energy levels are not overlapping and thus distinct emision peaks are present in the spectrum. In the solid and liquid phase b), the numerous occurring collisions smear out the different vibrational and rotational levels, resulting in energy bands which in turn leads to a broad emission spectrum.

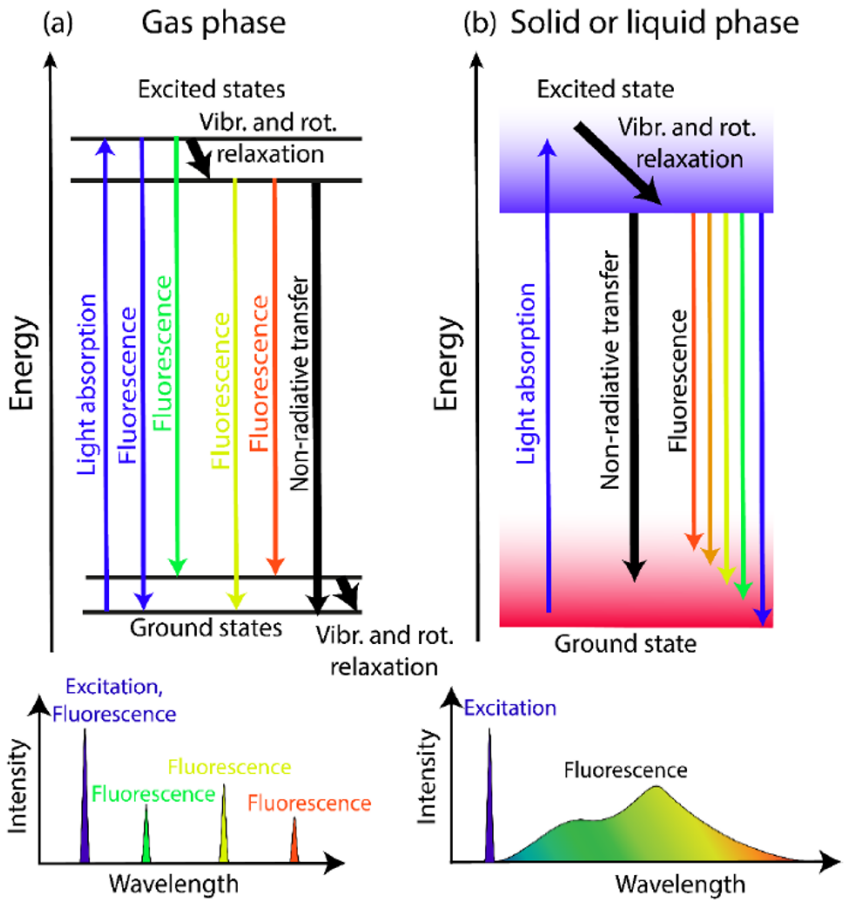

Figure 4: Energy level diagram showing absorption and fluorescent emission for gases a) and solid or liquid phase b). Figure from [31]

With Laser induced fluorescence (LIF), certain transitions in a molecule can be probed which makes this technique species sensitive and an important technique in combustion diagnostics [29]. In addition, LIF can be used to determine temperature, since the signal strength depends on how populated the corresponding energy levels are which in turn depends on the Boltzmann distribution [34]. In lidar measurements, fluorescent emission can be exploited to track tagged insects [27] or to measure the fluorescence emission of chlorophyll in vegetation [7].

3 Instrumentation

In this section, the different parts of the elastic hyperspectral lidar (EHSL) is described. In figure 5 the setup is depicted with the main unit (fig. 5 a)) including all the components of the EHSL. During the measurements, the baseline is mounted on a tripod.
The beam expander in figure 5 b) diverges, expands and collimates the laser beam from the fiber. The spectral analyser (fig. 5 c)) disperses the light in photon energy and at the same time determines the range. The different parts will be discussed in more detail in the further course of this chapter.

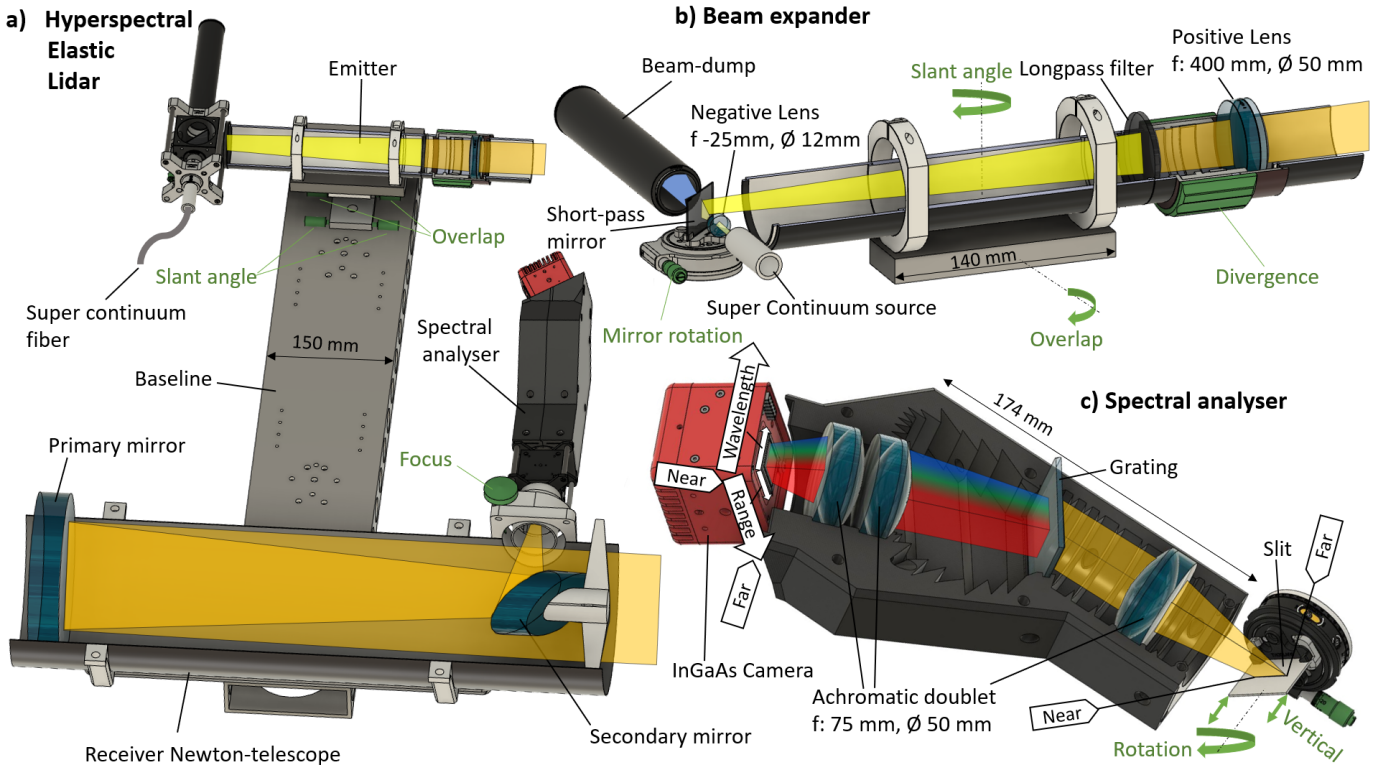

Figure 5: Assembly of EHSL with the main unit a) which is including a beam expander b) and a spectral analyser c). The beam expander diverges, expands and collimates the laser beam from the fiber while the purpose of the spectral analyser is to infer spectrum and range. Color coding; grey: opto-mechanics, green: degrees of freedom for alignment, yellow: broad band light cones.

3.1 Scheimpflug lidar method

In photography, the range in which the image is sufficiently sharp is termed depth of field (DoF). In conventional cameras the DoF is limited to a certain range and increases with decreasing aperture size. A pinhole camera therefore exhibits an infinite DoF. However, due to the small aperture size, long exposure times are required in order to acquire enough light. The Scheimpflug principle, on the other hand, exhibits infinite DoF along a line. This is achieved by tilting the detector with respect to the collection lens. In figure 6, Photoshop

was used to illustrate the effect of the different imaging principles. In figure 6 (a) the DoF is limited to the dog while objects in the front and back are blurry. In figure 6 (b) the pinhole gives infinite DoF, however, due to the long exposure time the moving dog is blurry. Figure 6 (c) is sharp along the entire path and besides, the moving dog is also sharp.

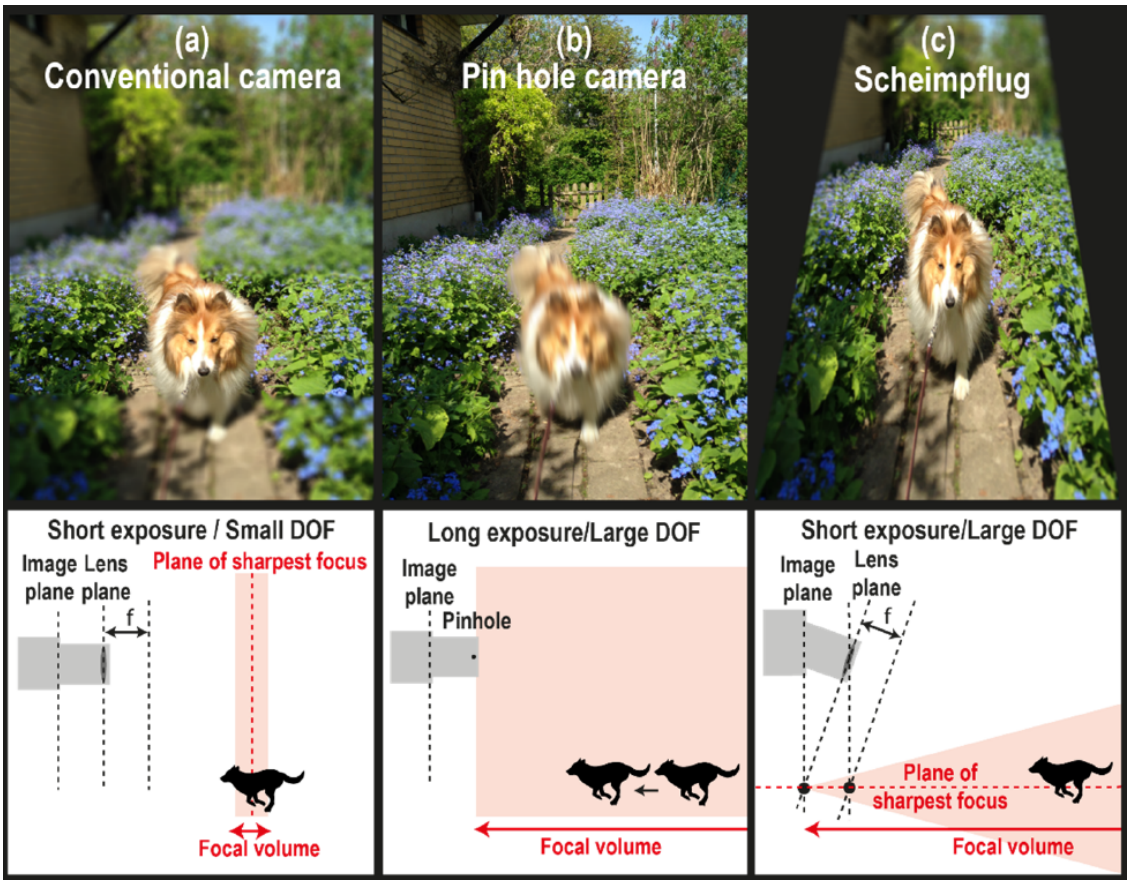

Figure 6: Comparison of Scheimpflug principle c) with a pin hole camera b) and a conventional camera a). Photoshop was used to point out the effect. Figure from [31]

The Scheimpflug principle was first described by J.Carpentier in 1901 [35] and further developed by T.Scheimpflug [36] [37] who introduced the hinge condition which is an additional constraint on how to tilt the lens depending on its focal length. The Scheimpflug condition, obligates the detector- and lens-plane to intersect on the object plane. For the hinge condition, the lens plane that is tilted in such a way that it is parallel to the detector, intersects with the front focal plane of the lens on the object plane.
The complete principle including Scheimpflug and hinge condition is portrayed in figure 7. If these conditions are fulfilled, each point along the object plane that lies within the FoV, is focused on the detector. The object plane in this case is a laser beam. The light that is detected is the backscatter from objects that cross the laser beam. Mathematical derivations of the Scheimpflug principle are found in [38], [22] and [23].

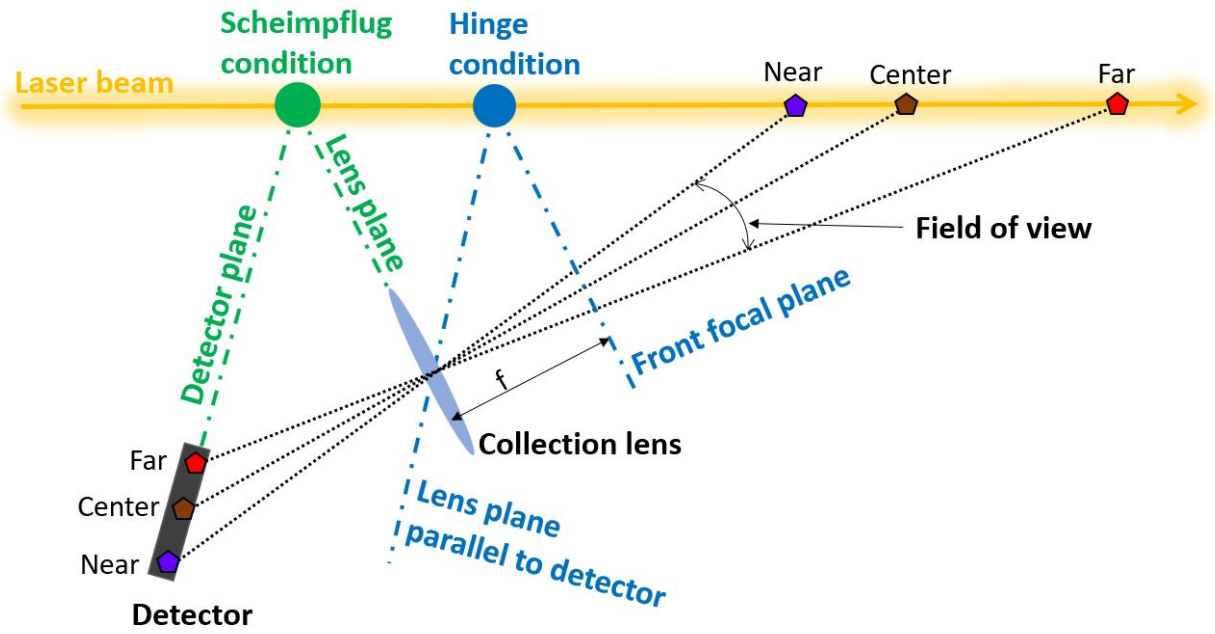

Figure 7: Scheimpflug and hinge conditions applied on a lidar. Within a certain field-of-view, each point along the object plane (laser beam) is focused on the detector.

Since in this thesis not only range but also the spectrum is to be determined, an additional unit to analyse the spectrum needs to be added. The spectral analyser combined with the Scheimpflug principle is depicted in figure 8.
The detector from figure 7, is replaced by a tilted entrance slit where the light from the object plane is focused. The range information is now contained along the slit and will be projected on the detector, the same way as is the first step when the object plane was projected on the slit. This implies that the Scheimpflug and hinge rules have to be applied twice. This concept was derived from previous works, see [7],[27], [28],[39].

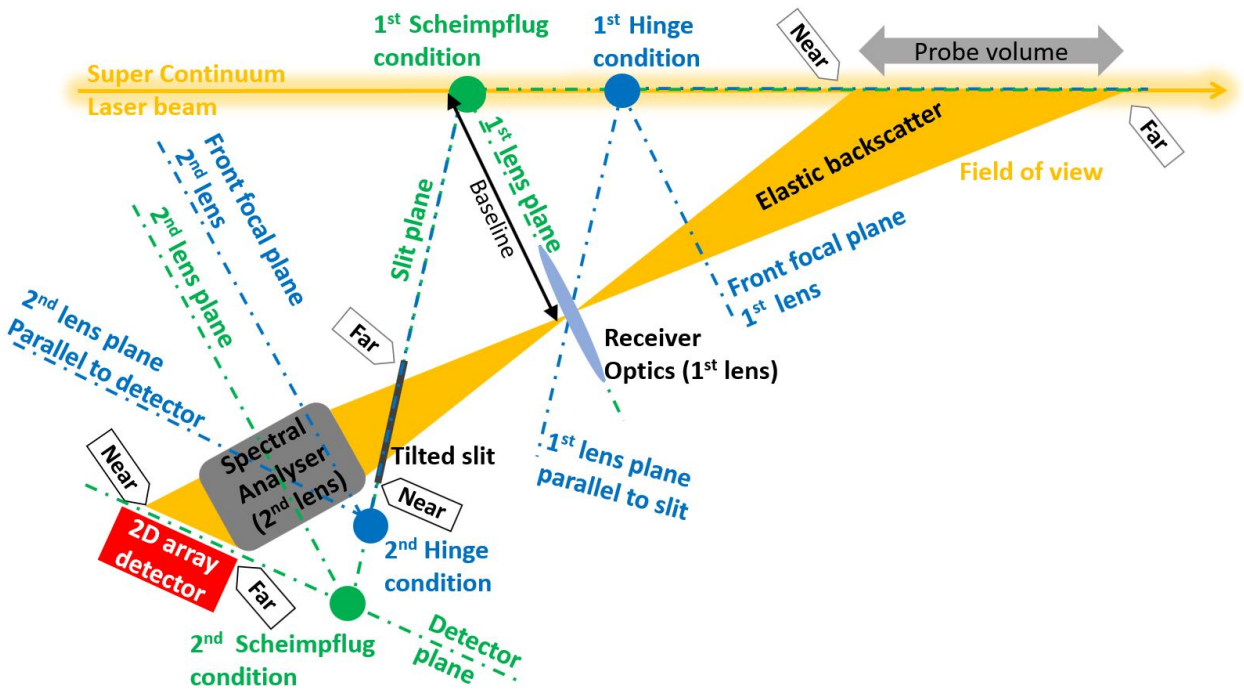

Figure 8: Scheimpflug and hinge conditions applied on a hyperspectral lidar. Both conditions are applied twice, first to project the object plane onto the slit and then to project the slit onto the detector.

3.2 Super continuum light source

Supercontiuum light is broadband light which is generated from femtosecond pulses from a mode locked, diode pumped solid state laser (DPSS), that propagate through a single mode fiber. The power density in single mode fibers is relatively high due to the small aperture size. The pulses generate nonlinear effects such as self-phase modulation (SPM) and Raman scattering [40], whereby the pump light at 1064 nm is broadened in photon energy and time. SPM is a third order nonlinear effect and is a result of the optical Kerr-effect which changes the refractive index n as a function of intensity of the electric field. In a Gaussian beam the intensity is higher in the center of the beam which results in a higher n in the center. The beam is thus creating its graded index (GRIN)-lens. This phenomena is known as self-focusing. In the temporal domain, self-focusing induces a change in phase which is known as self-phase modulation. SPM leads to a chaotic broadening of the spectrum. Hence, a pulse that propagates through a third-order nonlinear medium changes its spectrum. A more detailed description of SPM is found in the chapter nonlinear optics in [30].
Raman scattering is an inelastic scattering mechanism discussed in chapter 2. The inelastically scattered light results in a broadening of the spectrum.
The source used in this work is a Supercontiuum fiber laser (SC400 Fianium, Nordiske Kabel og Trådfabriker (NKT), Denmark) with a spectral range from 400 nm − 2400 nm (see figure 9). The wavelength of the pump is at 1064 nm, generated by mode-locked DPSS Nd:YAG laser with a repetition rate of 80 MHz, a pulse duration of 400 fs and a max pulse energy of 50 nJ.

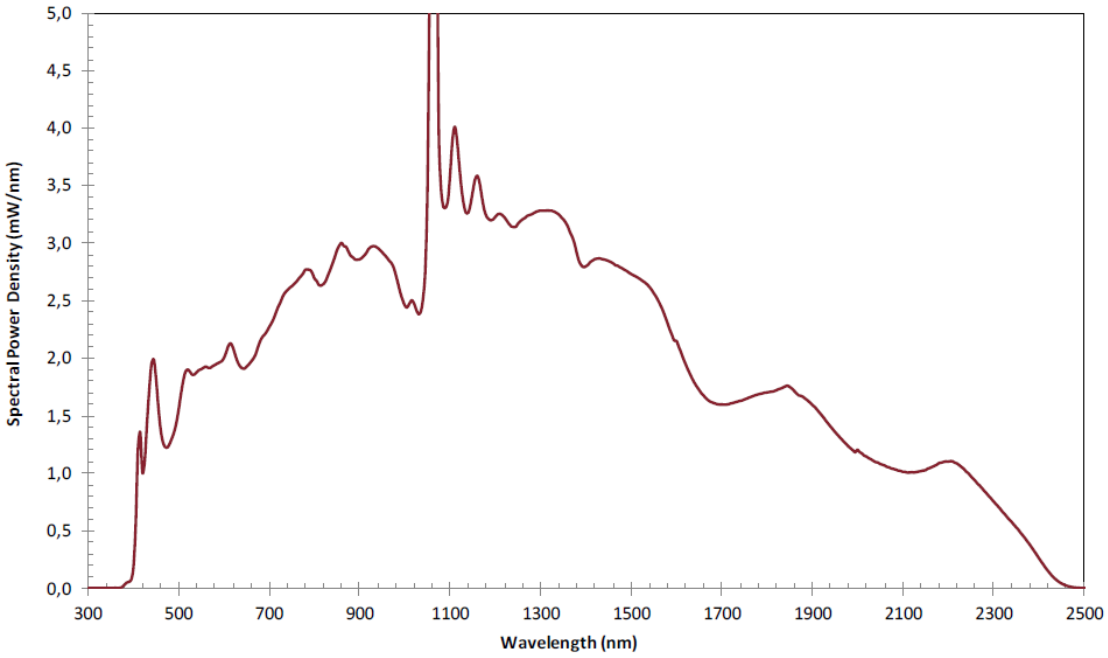

Figure 9: Broadband spectrum of the supercontiuum fiber laser SC400 Fianium, (Nordiske Kabel og Trådfabriker (NKT), Denmark). Figure taken from datasheet, NKT.

3.3 Beam expander

In figure 5 b), the setup of the beam expander used in the EHSL is depicted. The purpose of the beam expander is to expand the beam of the supercontinuum source and strip off the visible part of the spectrum. The beam expander is desigend with a Galilean telescope composition where first a negative lens ($f = -25\,\text{mm}$, $\phi = 12\,\text{mm}$, LC1054-B-ML, Thorlabs, USA) is used to expand the beam and afterwards collimate it with a positive lens ($f = 400\,\text{mm}$, $\phi = 50\,\text{mm}$, ACT508-400-B-ML, Thorlabs, USA). A dichroic mirror (SP 650 nm, 25x36 mm^2, Thorlabs, USA) reflects wavelengths longer than 650 nm, while shorter wavelength are transmitted and disposed in a beam-dump. In addition to the dichroic mirror, a longpass filter (RG850 Schott, $\phi = 50\,\text{mm}$, Edmund Optics, UK) strips of light shorter than 850 nm, resulting in a emitted spectral range of $850\,\text{nm} - 2400\,\text{nm}$ and an average power of $\approx 3\,\text{W}$. The beam expander is mounted on a tangential stage (Stronghold, Baader Planetarium, Germany) with which the slant and overlap angle can be adjusted. The overlap angle is adjusted until laserbeam and field-of-view (FoV) of the receiver overlay. The slant angle is used to adjust the angle between laser and FoV to fulfill the Scheimpflug and Hinge conditions (see section 3.1) and to define the scope of the range.

3.4 Receiver

A Newton telescope ($f : 800\,\text{mm}$, $\phi = 200\,\text{mm}$) is used to collect the backscattered light. The collected light is then focused onto slit of the spectral analyser. The telescope is mounted on the lidar-baseline together with the emitter (see fig. 5 a)) on a fixed dovetail mount. The

focus can be adjusted with the focus-knob, see figure 5 a).

3.5 Spectral analyser

The spectral analyser is mounted on the Newton telescope. It disperses light by photon energy with a transmission grating.
Since the main goal of this thesis was to design the spectral analyser, a detailed description of the functionality and performance is found in chapter 4.

3.5.1 InGaAs detector

Silicon is the most frequently used semiconductor in cameras and detectors thanks to its abundance and pureness. With a bandgap of $E_g = 1.12\,\text{eV}$, silicon is sensitive up to $\approx$ 1110 nm. Photons at longer wavelength, however, will not have enough energy to overcome the bandgap.
Indium galium arsenide (InGaAs) is a ternary compound semiconductor which is obtained by combining the two binary compound semiconductors indium arsenide (InAS) and gallium arsenide (GaAs). The bandgap is given by the mixing ratio of InAs ($E_g = 0.36\,\text{eV}$) and GaAs ($E_g = 1.42\,\text{eV}$) [41]. A typical bandgap energy in InGaAs devices is $E_g = 0.75\,\text{eV}$, which allows the detection of photons up to $\approx 1654\,\text{nm}$. Another common InGaAs variety is able to detect photons up to $2.2\,\mu\text{m}$, which however, exhibits a lower quantum yield.
The drawback of InGaAs compared to Si is the significantly higher price.
The camera used in the spectral analyser is a 2D-InGaAs detector (C-RED3, FirstLight, France) with 640x512 pixels^2 and a pixel pitch of $15\,\mu\text{m}$. The quantum efficiency is depicted in figure 10 for two different temperatures.

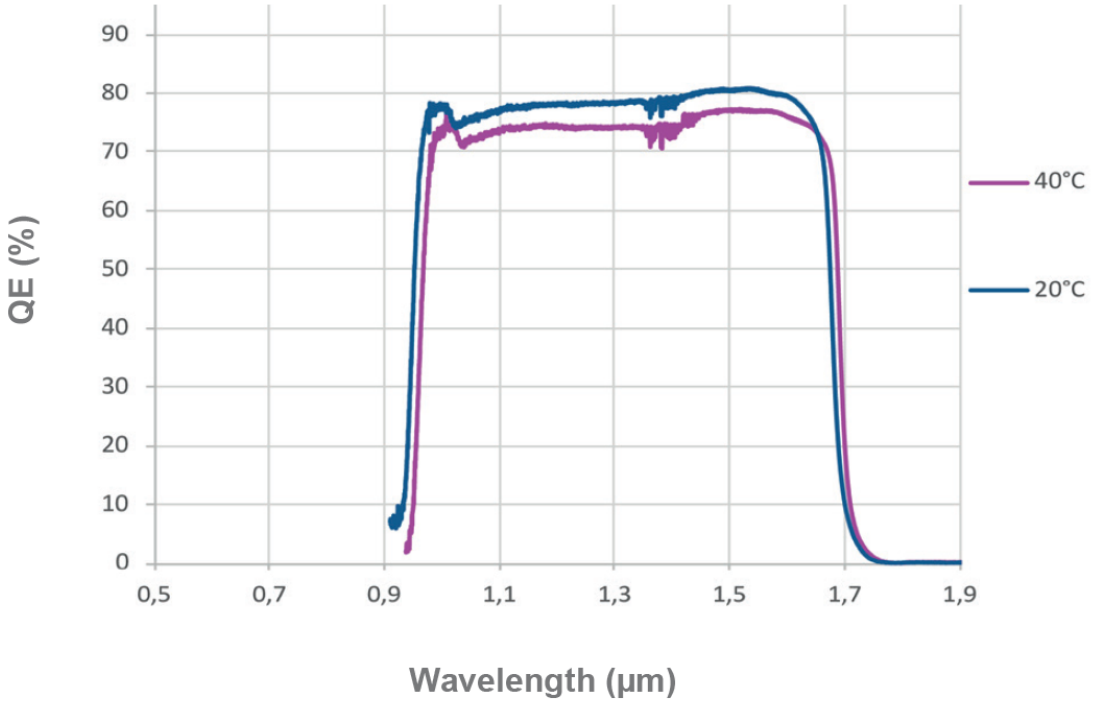

Figure 10: Quantum efficiency (QE) at two different temperatures of InGaAs-camera (C-RED3, FirstLight, France). Figure taken from datasheet, FirstLight.

3.6 Hyperspectral data cube

The hyperspectral lidar is recording backscattered light intensity (16 bit) as a function of range and photon energy in single exposure of a 2D-detector. The time is recorded by stacking consecutive exposures. The hyperspectral images are stored in a data cube where the axes are range, wavelength and time, respectively. A Labview script records the hyperspectral data cubes and stores them as raw files with a time stamp. An illustration of a system specific hyperspectral datacube is shown in figure 11. The spectrum spans from approximately 1000 nm − 1600 nm and the range from approximately 50 m − 108 m with the termination placed at 100 m. The span-width of the range is determined from the magnification of the spectral analyser as well as the field-of-view (FOV) of the receiver telescope. The start point of the range is determined by the overlap of the laser with the FOV. With the slant angle, the range can be shifted in such a way that the termination is close to the border of the detector in order to exploit all the pixels. The pixel footprint increases with range as mentioned in chapter 4.

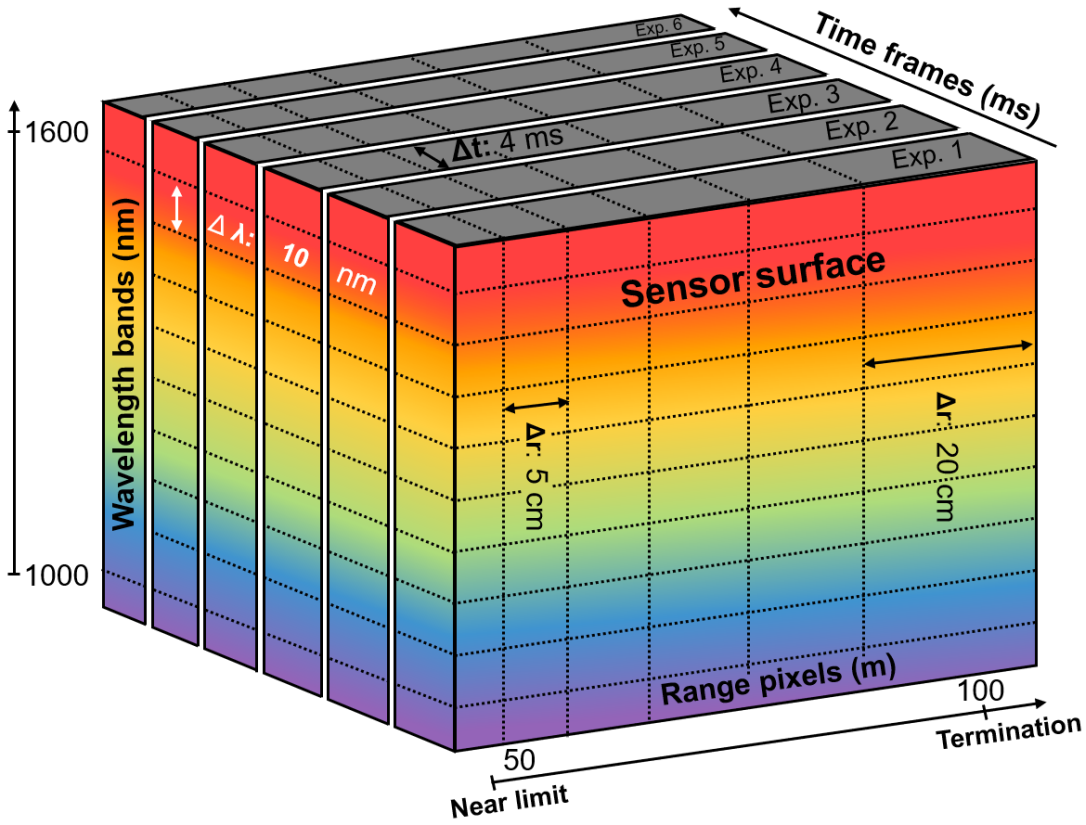

Figure 11: Illustration of the hyperspectral data cube recorded by the EHSL. The spectral range stretches from approximately 1000 nm − 1600 nm and the range from approximately 50 m − 108 m with the termination placed at 100 m. Figure adapted from [27]

4 Spectral analyser design

This section describes the different procedures when designing and building the spectral analyser. The different steps are designing of the optical system with raytracing software (Zemax, Ansys, USA), designing the opto-mechanical setup with computed aided design (CAD) (fusion 360, Autodesk, USA) and eventually 3D-printing and assembling the spectral analyser. Figure 12 is a illustration of the CAD-design including the raytracing simulation.

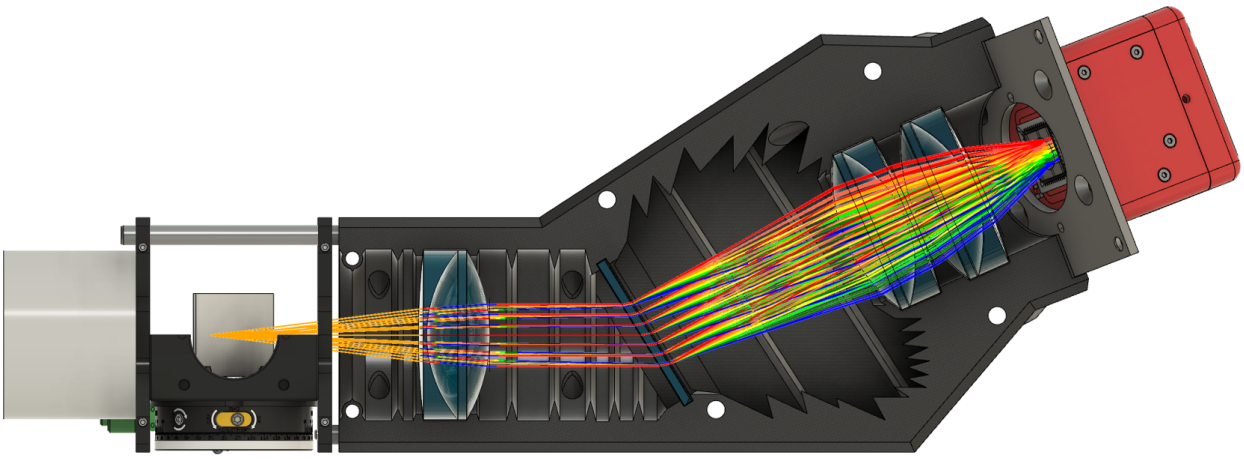

Figure 12: CAD-design of spectral analyser including the raytracing simulation.

4.1 Spectral dispersion

The spectral analyser disperses light in photon energy by means of a blazed transmission grating. Different wavelengths of a collimated beam will be dispersed at different angles according to the grating equation 3. With equation 3, the angle at which a certain wavelength λ will be dispersed can be determined,

$$m\lambda = \Lambda(\sin\theta_{\text{in}} + \sin\theta_m), \tag{3}$$

where m is the diffraction (integer number) and Λ is the separation between grooves. θ_{in} is the incident angle of the collimated beam and θ_m the dispersion angle of a given diffraction order m.
The resolving power R is a measure of how small wavelength separations can be distinguished and is directly proportional to the number of lines N that are illuminated (see eq. 4).

$$R = N \cdot m \tag{4}$$

A blazed grating is furthermore optimized to maximise the energy in a specific order, mainly by decreasing the intensity in the 0^{th} diffraction order.

A typical setup for a transmission blazed grating is depicted in figure 13. The incident angle θ_{in} must match the blazing angle θ_{Blaze} to achieve maximal grating efficiency in the required order. The required spectral range $\Delta\lambda$ is given by the angle difference $\Delta\theta$, between λ_{short} (blue) and λ_{long} (red). An expression to determine $\Delta\theta$ is given in equation 5 and is simply derived from the grating equation 3.

$$\Delta\theta = \sin^{-1}\left(\frac{m\lambda_{\text{long}}}{\Lambda} - \sin\theta_{\text{in}}\right) - \sin^{-1}\left(\frac{m\lambda_{\text{short}}}{\Lambda} - \sin\theta_{\text{in}}\right) \tag{5}$$

A focusing lens is used to convert the incident propagation angles θ_1 at $m = 1$ into positions on the detector. With $\Delta\theta$ and the geometrical width w of a detector array, the required focal length f_{foc} of the focusing lens can be determined,

$$f_{\text{foc}} = \frac{w}{2 \cdot \tan\left(\frac{\Delta\theta}{2}\right)}. \tag{6}$$

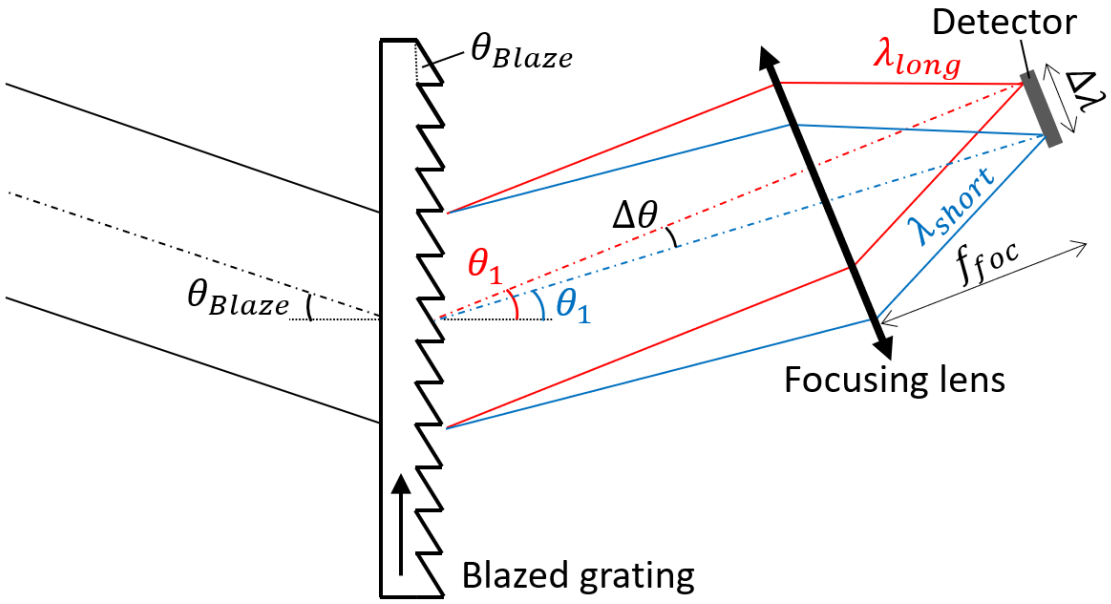

Figure 13: Setup to spectrally resolve collimated light using a transmission blazed grating, a lens and a detector array. The dispersion angle θ_1 at $m = 1$ is drawn for λ_{short} (blue) and λ_{long} (red). The black arrow pointing upwards is the blaze direction and is specifically defined by the manufacturer Thorlabs, USA.

The camera for the spectral analyser in this work is an InGaAs camera from FirstLight (see section 3.5.1) with a geometrical sensor width of $w = 7.68\,\text{mm}$. A spectral range of $\Delta\lambda \approx 600\,\text{nm}$ ($1000\,\text{nm} - 1600\,\text{nm}$) is selected to exploit the sensitivity from the InGaAS sensor (see fig. 10).
In order to achieve the required spectral range, a transmission grating with a groove frequency of $\frac{1}{\Lambda} = 300\,\text{grooves/mm}$ (GTI50-03A, Thorlabs, USA) is chosen and thus f_{foc} has to be $\approx 42\,\text{mm}$.

4.2 Raytracing

As discussed in figure 8, the tilt and position of the detector have to fulfill the second Scheimpflug and hinge condition. These conditions, however, are a theoretical approach and are based on thin-lens approximations. In a optical setup as shown in figure 14 b), the lenses are far from thin. Hence, an optical raytracing sofware (Zemax, Ansys, USA) is exploited to determine the exact position of the detector.

The required focal length of the focusing lens $f_{\text{foc}} \approx 42\,\text{mm}$, which was calculated in section 4.1 is achieved by using two achromatic doublets with focal length $f = 75\,\text{mm}$, diameter $\phi = 50\,\text{mm}$ and with an SWIR-anti reflection (AR) coating from $1050\,\text{nm} - 1700\,\text{nm}$ (AC508-075-C, Thorlabs, USA). The two lenses with $f = 75\,\text{mm}$ form together the focusing lens unit with an effective focal length of $f_{foc} = 37.5\,\text{mm}$. Attaining the required focal-length with two lenses instead of one, reduces the lens surface curvature which is beneficial to reduce spherical aberrations. Furthermore, the availability of SWIR-AR coated, $\phi = 50\,\text{mm}$, off-the-shelf optics with $f < 50\,\text{mm}$, is very limited. The distance between grating and focusing lens is chosen such that the 0^{th} diffraction order can be separated for beam dumping.

Zemax features a merit function tool which allowed optimising the system with the goal of achieving the smallest spot size in the range direction δr. The variables that were adjusted by the merit function are lens separations, position and tilt of the detector.
A weight function was introduced to optimise the system to perform best in the far range since the pixel footprint increases with range and thus the impact of a large spot size is greatest at far distances. A thorough explanation for the resolution-range behaviour is found in [31],[23].

The result of the optimisation can be observed in the spot-diagram in figure 14 a) as well as in figure 15 a) where the root mean square (RMS, δr) is plotted as a function of wavelength for three different range positions. δr is to be as close to the pixel size of $15\,\mu\text{m}$ as possible. A smaller spot-size will not result in a better performance.
The RMS in the spectral direction ($\delta\lambda$) is limited by the slit width of $d = 200\,\mu\text{m}$. With the magnification $M = 0.5$ which is discussed below, the minimal spectral width on the detector side is $d \cdot M = 100\,\mu\text{m}$. Thus, $\delta\lambda$ being smaller than $100\,\mu\text{m}$ will not increase the spectral resolution. In the near range, however, $\delta\lambda > 100\,\mu\text{m}$, which is mainly due to field curvature caused by the focusing lens.

Different aberrations occur in the system and reduce its performance. The different aberrations are explained in detail in the chapter aberrations in [32]. Field curvature is one of the main contributors in this system and was compensated in the far range by tilting the detector, at the expense of increasing the spot-size in the near range. Another relatively large contributor is spherical aberrations which is increased in the far and near range where the rays are shifted from the optical axis. Best form lenses exhibit a non-spherical surface curvature which is designed to reduce spherical aberrations. In this system, however, due to the lack of low cost 50 mm best form lenses in the SWIR range, spherical lenses were used. Coma is mainly present in the far and near range where the rays enter the focusing lens at a certain angle (see fig. 15b)). This type of aberration is compensated to a certain extent for the far range while being enhanced in the near due to the tilt orientation of the detector. Chromatic aberrations are compensated by using achromatic lenses. The use of achromatic focusing lenses in conventional spectrometers is not essential since the detector can be tilted to almost entirely compensate for chromatic aberrations. However, in this system not only spectrum but also range is resolved. As can be observed in figure 14 a), a given wavelength, for example 1050 nm, is shifted upwards when going from far to near range. This effect is known as smile-effect and would require a different tilt angle for different range positions, which makes the use of achromatic lenses still useful. Detailed descriptions of how to design

a spectrometer can be found in [42],[43].

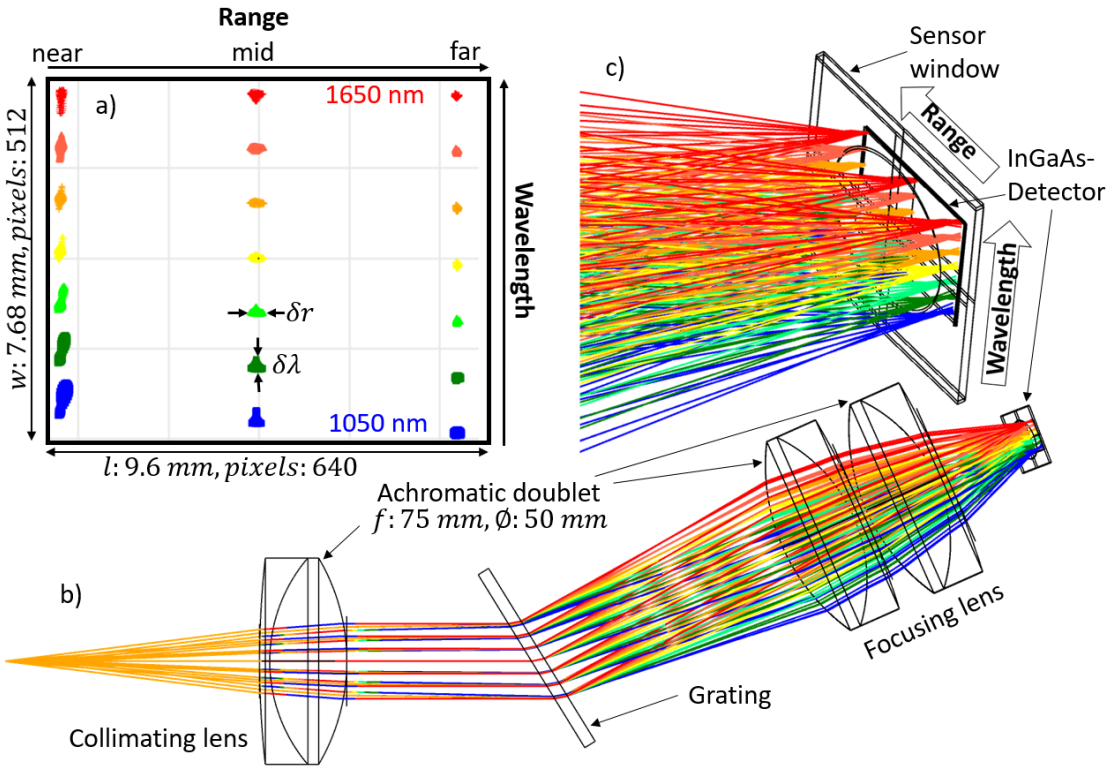

Figure 14: Raytracing simulation of the spectral analyser b) with rotated close-up view of the detector c). The system is optimised to perform best in the far range which can be seen in the spot-diagram a).

The magnification M in a optical 4-f system is defined as

$$M = -\frac{f_{foc}}{f_{col}} = -0.5. \tag{7}$$

With a given detector length $l = 9.6\,\mathrm{mm}$, the length of the entrance slit simply is,

$$\frac{l}{|M|} = 19.2. \tag{8}$$

The slit is tilted 45 ° to fulfill the first Scheimpflug and hinge condition (see fig. 8).

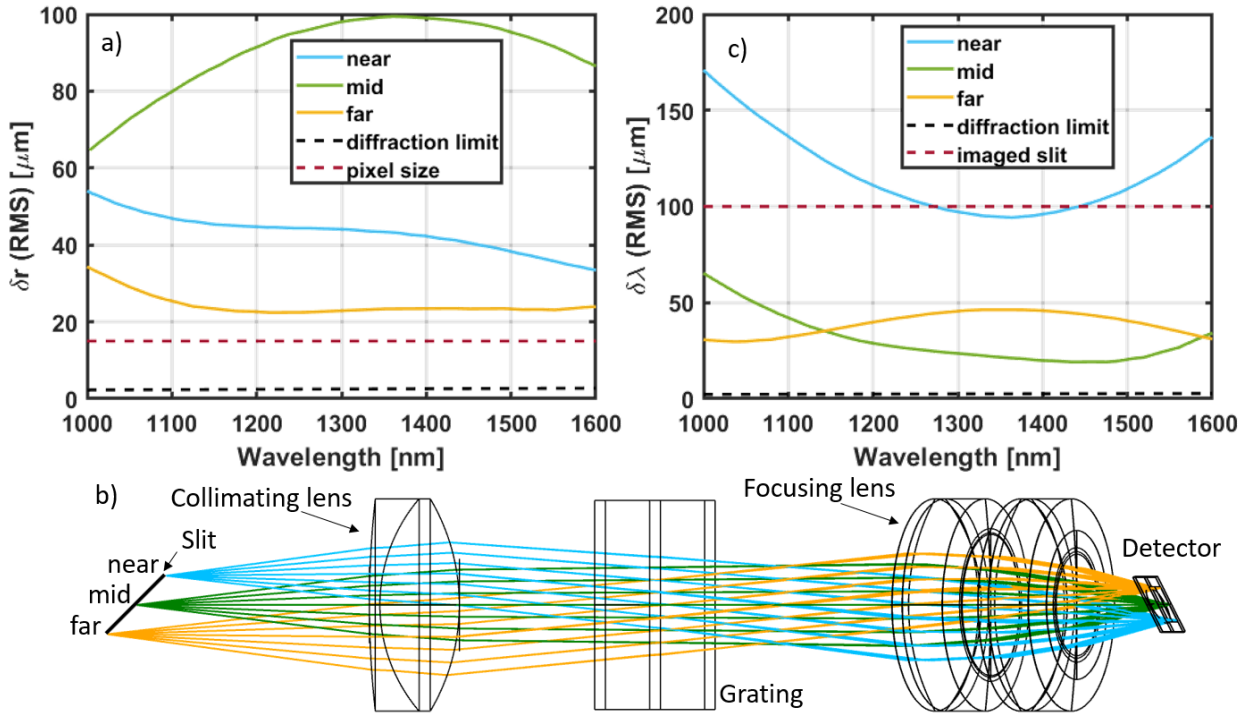

Figure 15: b) Raytracing simulation of the spectral analyser. a)c) RMS values of the spot-size diagram in figure 14 a), plotted as a function of wavelength at different range positions. Note that the values for δr and $\delta\lambda$, are referred to the spot size on the detector and are not range and spectral resolutions of the system.

4.3 CAD-design

In figure 16 the CAD-drawing of the spectral analyser is depicted. With the raytraced optical system from section 4.2, an opto-mechanical mechanical system was designed with CAD (fusion 360, Autodesk, USA). The device is based on a 3D-printed sandwich structure combined with cage system elements from Thorlabs. Four rods (ERx, $\phi = 6\,\text{mm}$, Thorlabs, USA) connect the 3D-printed structure with the cage cube (CW4, 30 mm, Thorlabs, USA) using two cage plate adapters (LCP4S, 30 mm to 60 mm, Thorlabs, USA). The tilted slit is mounted on a rotation stage (B4CRP M, Thorlabs, USA) with a filter holder (FFM1, Thorlabs, USA). The angle of the slit can be adjusted with the rotation stage. In addition to the angle, three adjustment screws allow vertical positioning. Furthermore, with the spacing between cage cube and 3D-print, the slit can be moved with respect to the InGaAs camera (C-RED 3, First Light, France) to adjust the focus. When focus is achieved, the rods can be locked with three lateral screws. The two 3D-printed parts are hold together with bolts, combined with threaded brass inserts which allow disassembling and reassembling in plastic material. The bolts and the rods furthermore act as a reinforcement structure to avoid deformation of the 3D-printed material. The camera is attached to the 3D-print with a milled aluminium camera adapter.

Baffles are included in the design at different positions along the optical path to reduce

stray light. Baffles block forward scattered light which becomes more significant at shallow grazing angles. Moreover, horn like structures were included to absorb the light from diffraction orders other than the first. Light from the 0^{th}- , 2^{nd}- and -1^{st}-diffraction order will be trapped in the beam-dumps and eventually absorbed [44]. The spectral analyser is installed on the receiver telescope with an aluminium telescope adapter.

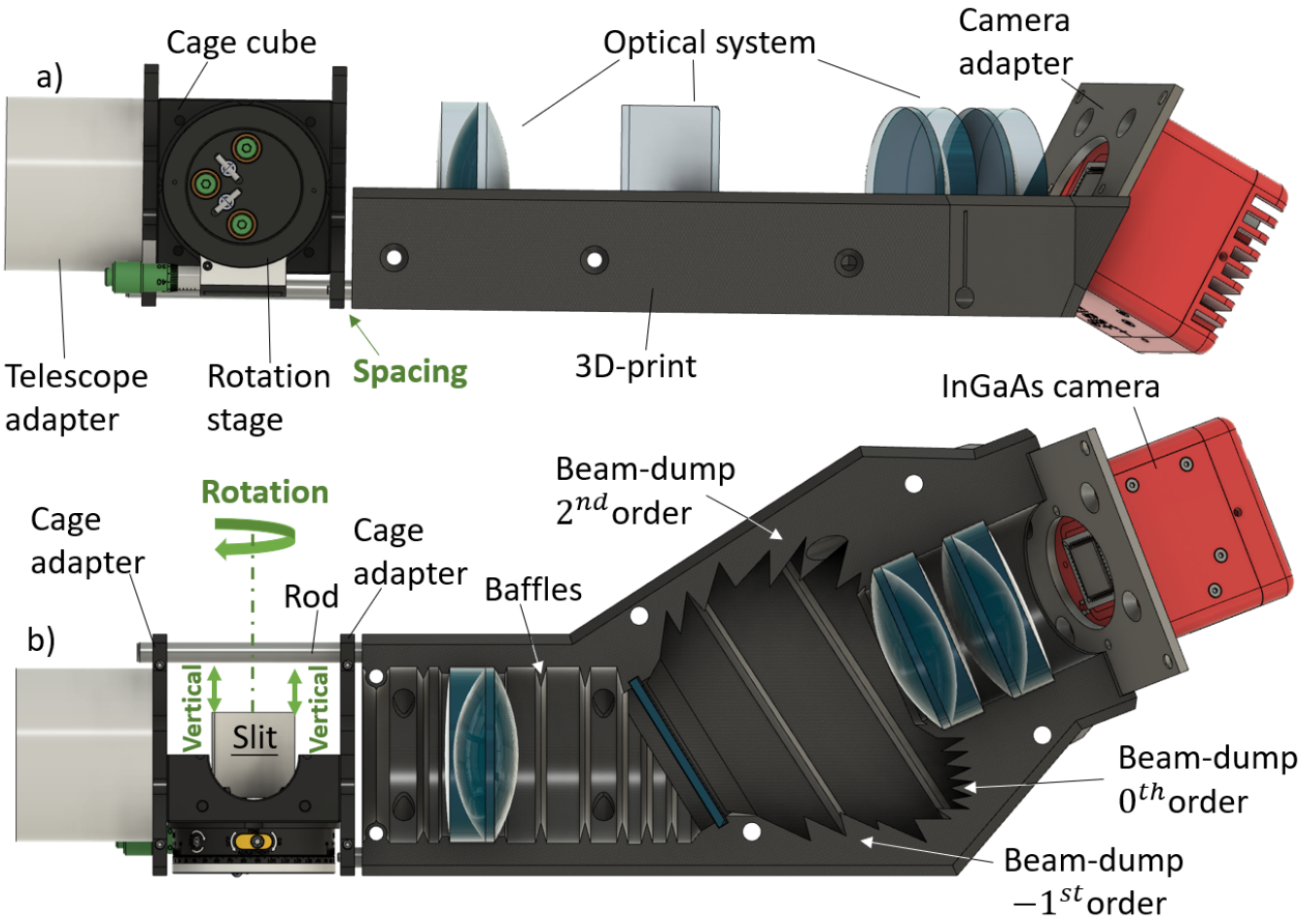

Figure 16: Sideview a) and topview b) of the spectral analyser designed in CAD (fusion 360, Autodesk, USA). Two 3D-printed bodies form together a sandwich structure (only the bottom is depicted) in which the optics is enclosed. The 3D-printed structure is complemented with different off-the-shelf components. The degrees of freedom for alignment are highlighted in green.

4.4 3D-printing

The designed sandwich structure discussed in section 4.3 was printed with a commercial 3D-printer (3D45, Dremel, USA) in black Polylactic acid (PLA-DF=02, Dremel, USA) with a fill factor of 20 % and a layer height of 200 μm. Figure 17 a) shows the bottom of the printed sandwich structure where all the optical and mechanical components are mounted. In figure 17 b) a photo of the fully mounted spectral analyser is depicted. The advantage of

3D-printing over CNC-machining is the ability of creating complex structures such as baffles and inner corner which are not possible with milling. In 3D-printing, however, overhanging structures have to be avoided. Inner diameters were designed with a positive tolerance of $\approx 0.2\,\text{mm}$ as the diameters tend to shrink during printing. The printing time of one piece was roughly 16 h.

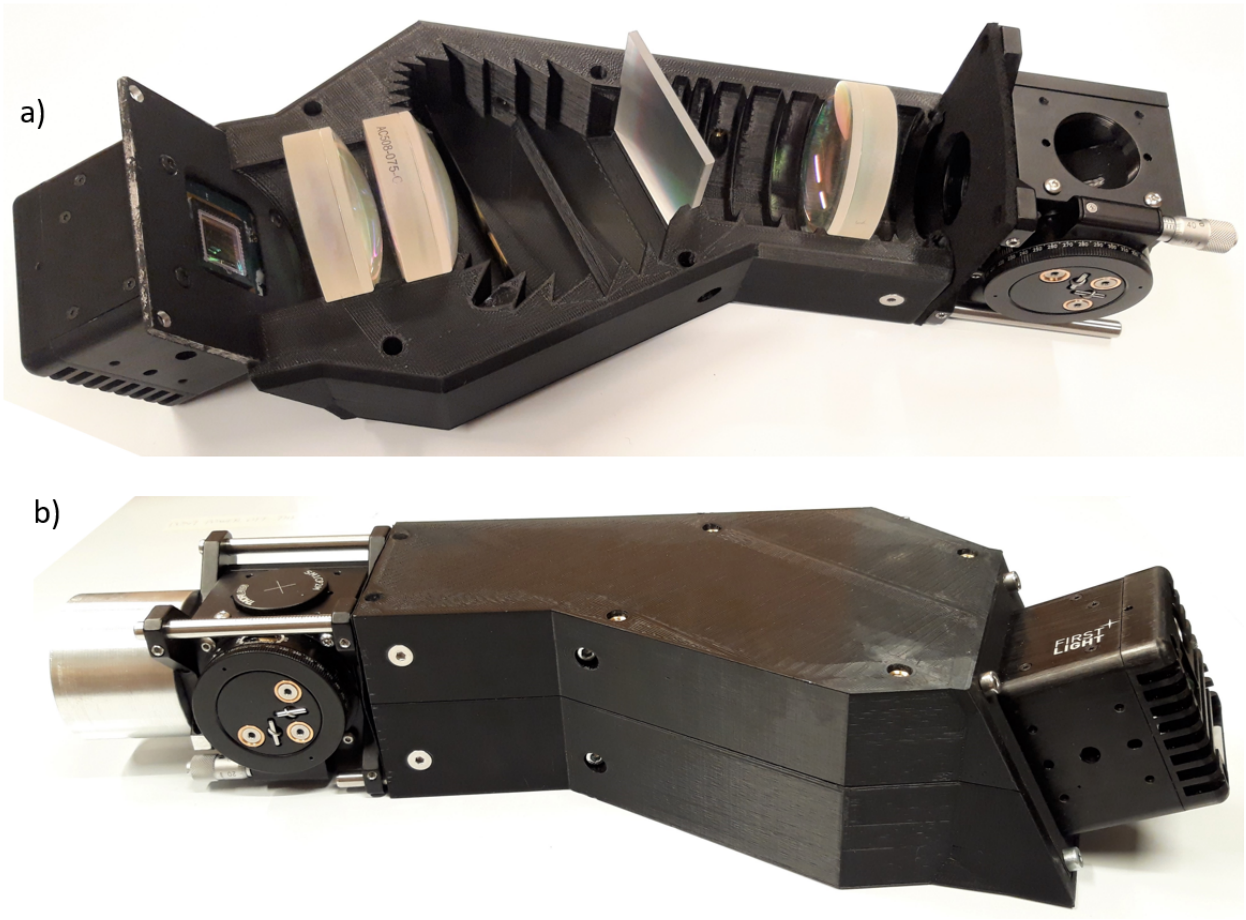

Figure 17: Photo of the 3D-printed spectral analyser. Panel a) is without the top part of the sandwich structure to make the optics visible while in b) the fully mounted spectral analyser is shown.

5 Spectral analyser characterisation

A pre-existing prototype (EHSL 1.0) was characterised and the required improvements were identified. The redesigned system (EHSL 2.0) was characterized equivalently for comparative analysis.

Both systems were characterised with the setup similar to figure 18. In order to illuminate the detector over the entire range, an integrating sphere, coated with $BaSO_4$ ($\phi = 200\,\text{mm}$, Oriel, USA) was used to uniformly illuminate the entrance slit of the spectral analyser. The uniformity of the illumination imitates light that comes from all possible range positions.

During the characterisation discussed below, a low pressure spectral Xenon lamp and a halogen tungsten light bulb were used as light sources.

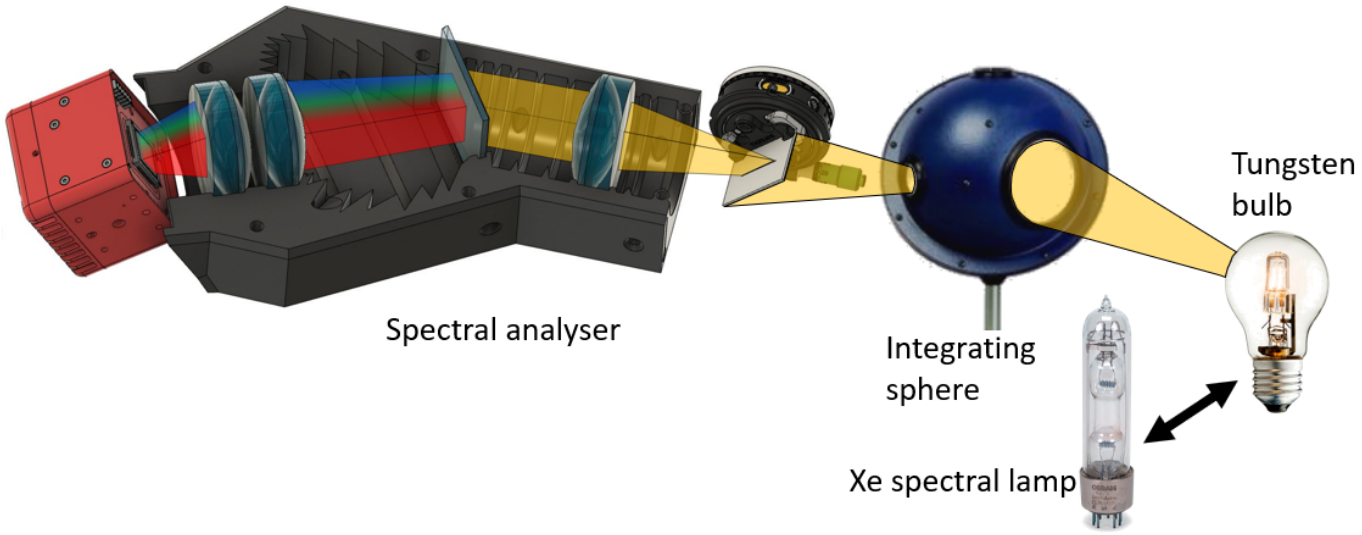

Figure 18: Setup to characterise the spectral analyser exploiting an integrating sphere to uniformly illuminate the slit. During the characterisation, a spectral Xenon lamp and a tungsten incandescence bulb were used as light sources.

5.1 Spectral analyser EHSL 1.0

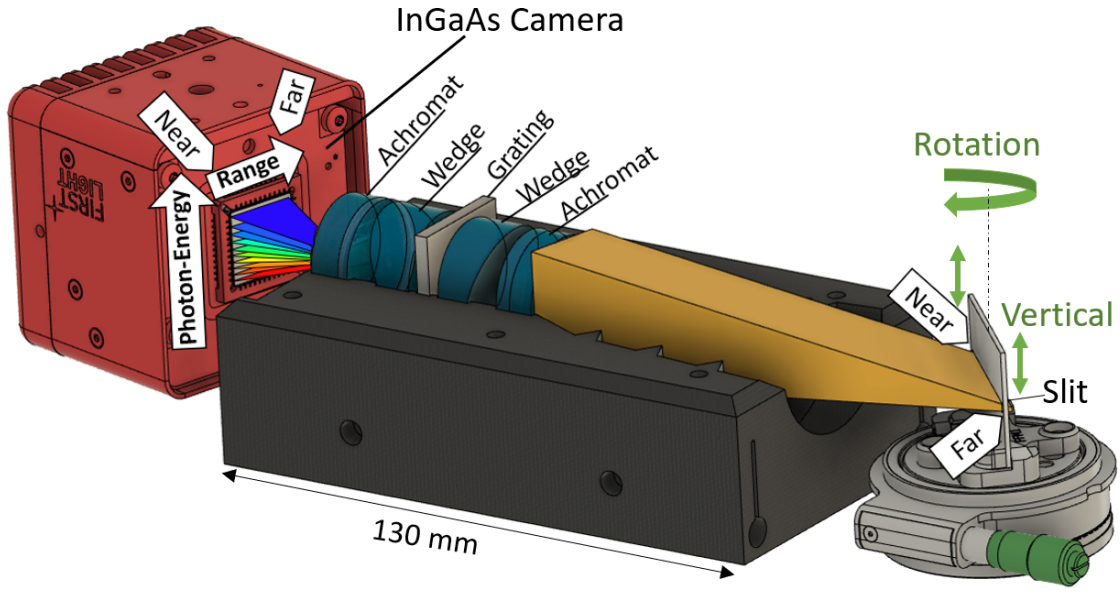

Figure 19: Spectral analyser of the EHSL 1.0 designed in the prism-grating-prism (PGP) method.

The EHSL 1.0 (fig. 19) was installed in the Scheimpflug lidar similarly to EHSL 2.0, which was described in figure 5. The main difference is the spectral analyser, which in the first prototype was designed in the prism-grating-prism (PGP) method [45]. The PGP design exhibits some advantages over the design in EHSL 2.0 in terms of size and compactness. However, for a spectral analyser in the short infrared (SWIR) regime, the availability of coated prisms with the required size is limited and the use of prisms would cause internal reflections and lead to ghosting effects.

In figure 20 a low pressure spectral Xenon lamp was used as a light source to calibrate the system.
Figure 20 a) shows a single exposure of the Xenon emission lines recorded with the spectral analyser. A high-pass filter was applied with Matlab to increase the visibility of the emission lines. Computing the mean value in each column reveals the measured spectrum of Xe (fig. 20 b)) where certain emission lines from the literature were assigned to the spectrum. With the assigned wavelengths and their pixel values, a first degree polynomial was fitted to convert the pixel value to a wavelength in nm. Figure 20 d) is the linear regression. From figure 20 a) it is evident that the spectral lines are bending along the range. This effect is referred to as smile. The bending along the wavelength is called keystone. Both, smile and keystone are mainly caused by distortion aberrations from the optics. In [46] a robust method how to characterise these effects is presented. In figure 20 c) the linear regression is plotted at different range positions, which is a slightly different method to characterise the smile effect. The change of the parameters b_0 and b_1 results from the bending of the spectral lines and can be used to quantify the smile effect. The artefacts between pixel 250 and 300 are no Xenon emission lines but might be caused by ghosting effects since the wedge prisms in figure 19 are uncoated. Ghosting happens from multiple partial reflections on several surfaces in a optical system.
Furthermore, it becomes evident from figure 20 a) that not the entire area of the detector is illuminated.

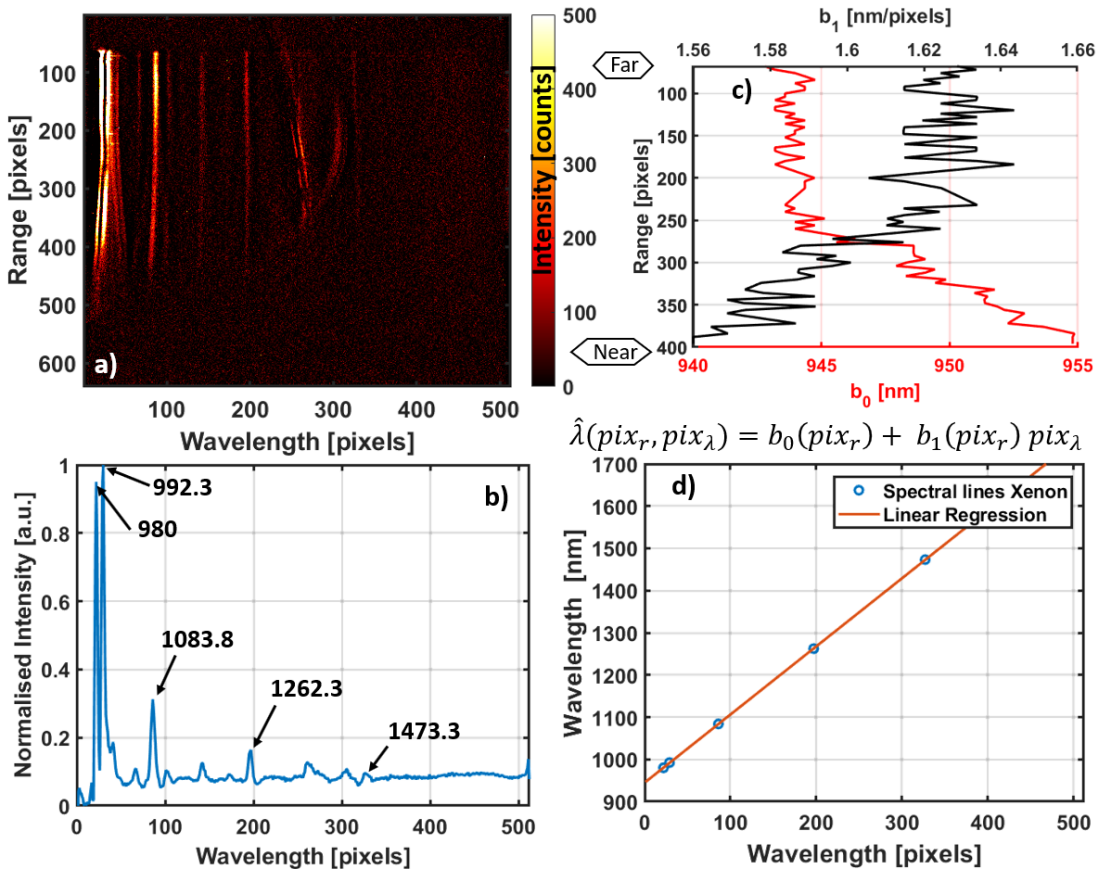

Figure 20: Spectral calibration using a Xenon-lamp. a) Spectral emission lines of Xe recorded with EHSL 1.0. b) Spectrum in the far range with the assigned values in nm. d) Linear regression to convert the pixel values to wavelengths in nm. c) Parameters of linear regression as a function of range.

In figure 21 and 22, a tungsten halogen light bulb is used as a light source to characterise the spectral sensitivity and flat field of the system. The light bulb is assumed to be a blackbody radiator at 3000 K. In figure 21, the measured spectrum of the halogen bulb (blue) is divided by the theoretical Plank spectrum (see eq. 14.4-9 in [30]) of a blackbody radiator at 3000 K (red), which results in the sensitivity curve of the system (orange). The decrease in sensitivity for longer wavelengths is due to the decrease in efficiency of the grating (purple). The camera responsivity curve is plotted in green and limits the sensitivity of the system at the margins of the spectral range.
Moreover, dips at ≈ 1200 nm and ≈ 1400 nm are present in the sensitivity curve. These dips are on the one hand caused by the $BaSO_4$ coating of the integrating sphere which exhibits a dip in reflectance at ≈ 1400 nm and on the other hand by OH inside the quartz glass of the halogen bulb. Hence, the dips arose during the calibration and will not limit the performance of the system.

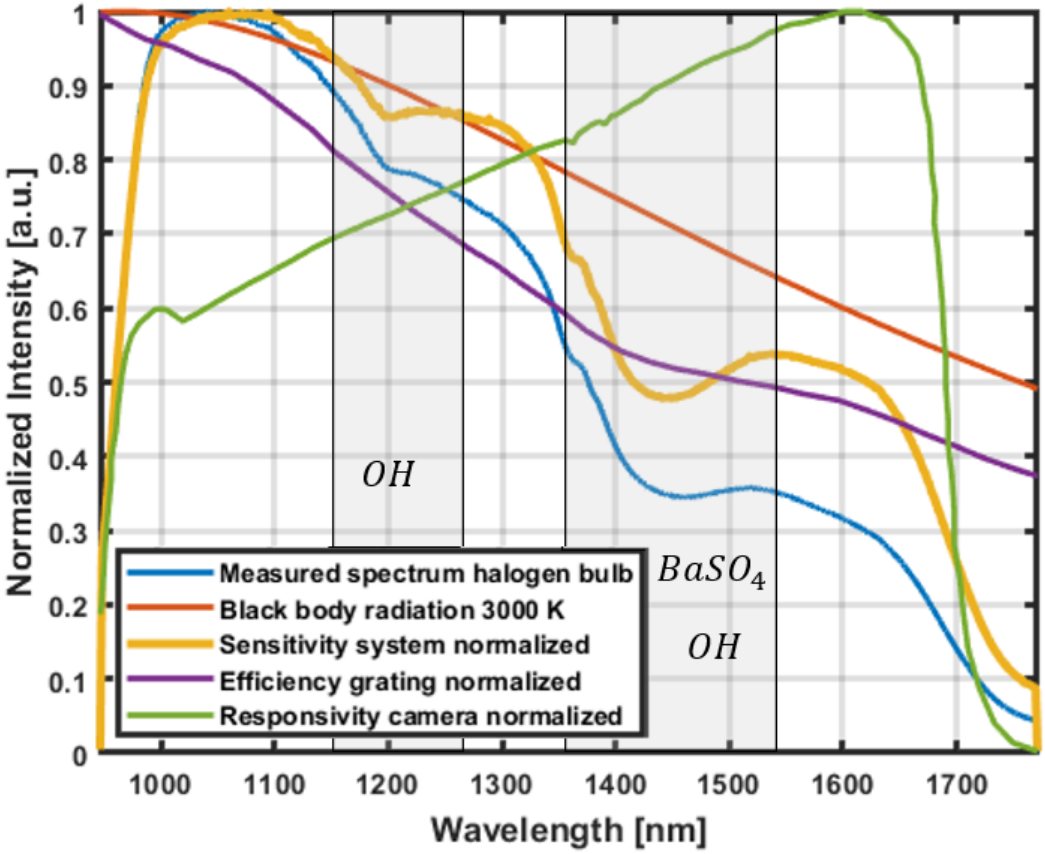

Figure 21: Spectral sensitivity plot of the EHSL 1.0 (orange), using the measured blackbody radiation of a halogen bulb (3000 K) (blue) which is compared to the theoretical black-body radiation at 3000 K (red). The grating efficiency (purple) and the camera responsivity (green) are plotted as well. The dips appearing in the sensitivity plot at ≈ 1200 nm and ≈ 1400 nm are caused by the BaSO4 coating of the integrating sphere and by OH from the quartz glass of the halogen bulb, respectively.

Figure 22 b) is the detector-image of the blackbody radiation of the halogen bulb. The illumination is expected to be uniform along the entire range owing the use of the integrating sphere. The shading of the detector that was suspected in figure 20 becomes even more obvious in figure 22 b), where the far and near range are entirely blocked from the illumination. In figure 22 c) a cross-section of the spectral analyser reveals how the cage adapter (blue hatched) blocks part of the light and moreover introduces a reflection-spike which is visible in the flat-field plot (figure 22 e)). Furthermore, part of the light that is not obscured by the cage adapter, is blocked by the 3D-print as the lens is to small. This is schematically illustrated in figure 22 d) with the far and near light cone which do not fully overlay with the collection lens. Hence, only the overlapping areas (green) are collected by the lens. The flat-field describes the sensitivity of the system as a function of range. For a uniformly illuminated slit, the flat-field is theoretically expected to be a top-hat profile. Since far and near range are obstructed from the illumination, the flat-flied plot of this system differs strongly from a top-hat profile. Figure 22 f) is a close-up view of the cage-adapter that is blocking the

light. Figure 22 a) shows the normalised spectral sensitivity at three different range positions within the illuminated area. The normalised spectral sensitivity doesn't change significantly for the different range positions a part from the far range which is slightly different for longer wavelengths.

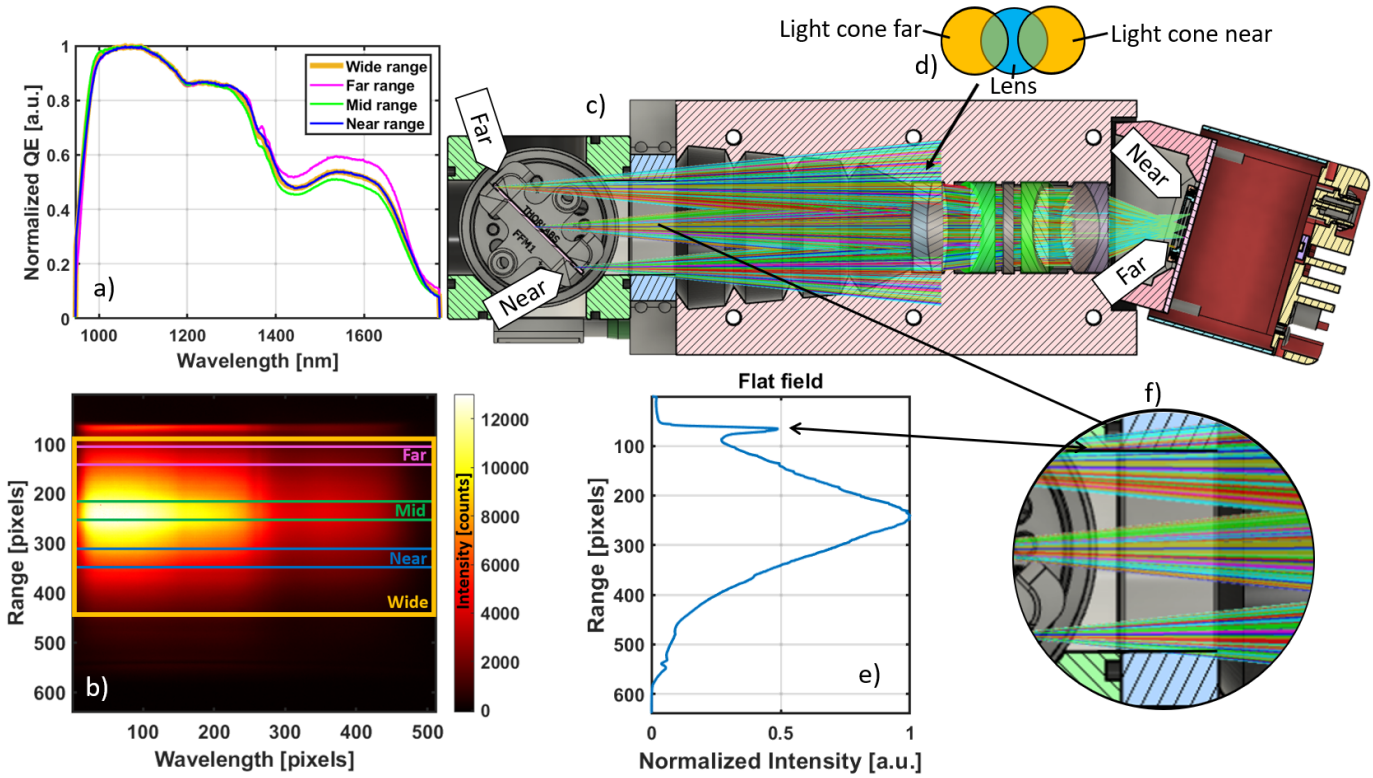

Figure 22: a) Spectral sensitivity plot of the EHSL 1.0, at three different range positions using the blackbody radiation of a halogen bulb. b) Detector-image with uniformly illuminated slit. e) Flat-field plot revealing the shading of the detector. c) Cross-section of the spectral analyser revealing how the cage adapter (blue hatched) and the 3D-print block light from the far and near range. d) Schematic illustration of how the lens only collects part of the near and far light cones. f) Is a close-up of the cage-adapter.

Different issues appeared during the characterisation of EHSL 1.0, which made a redesign of the first prototype necessary. The first issue which had to be addressed was the ghosting effects seen in figure 20 a), which are caused by the uncoated wedges. The use of wedges can be avoided by angling the grating and the camera accordingly. The second and more serious issue was the shading of the detector. The entire setup had to be scaled up, including optics and grating, to solve this issue.

5.2 EHSL 2.0

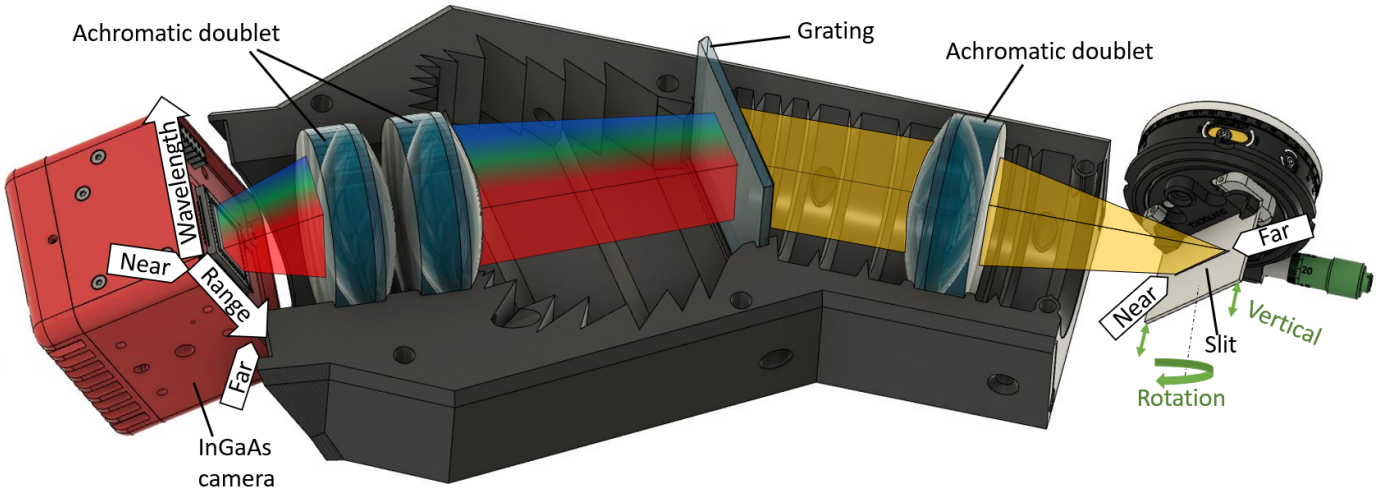

Figure 23: Spectral analyser of the EHSL 2.0 designed without the use of wedges.

The redesigned spectral analyser EHSL 2.0 is depicted in figure 23. The use of wedges was avoided and the optics was scaled up to solve the issues experienced in EHSL 1.0.
The spectral analyser had to be focused and aligned before starting the calibration measurements. The focus can be adjusted with the spacing between 3D-print and cage-cube (see fig. 16a)). A transparent plastic foil with a line pattern was placed in front of the entrance slit (inspired by [47],[48]) and the spacing was adjusted until the black lines were sharpest. Figure 24 a) shows the black lines of the line pattern. In 24 b), the intensity is plotted along the range, featuring the line pattern. As discussed in chapter 4.2, the optical system is designed to perform best in the far range and lowest in the near, which can be observed in figure 4.2 a) and b).

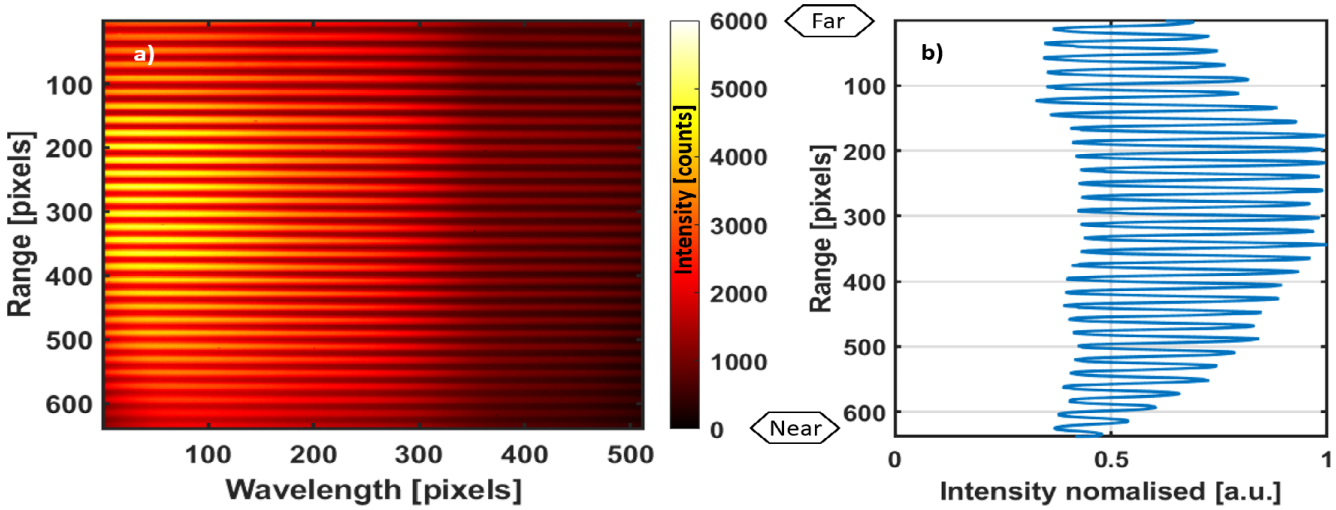

Figure 24: a) Detector-image with line pattern in front of the entrance slit to adjust focus, using a halogen bulb as a light source. b) Intensity plotted as a function of range. Note that the system is optimised to perform best in the far range.

In order to compare the performance of the redesigned system with the first prototype, the EHSL 2.0 was characterised in a similar manner as the EHSL 1.0. Hence, the description of the calibration procedure is found in section 5.1.
Comparing figure 25 with the equivalent figure 19 from the first prototype, it is obvious how the spectral lines now stretch over the entire sensor and no ghosting effects are visible. The smile effect is difficult to compare as in EHSL 1.0, the emission lines do not appear over the entire range. The FWHM of the spectral line at 1473.3 nm is 8 pixels which corresponds to a spectral resolution of ≈ 9.5 nm in the far range, resulting in 64 effective spectral bands.

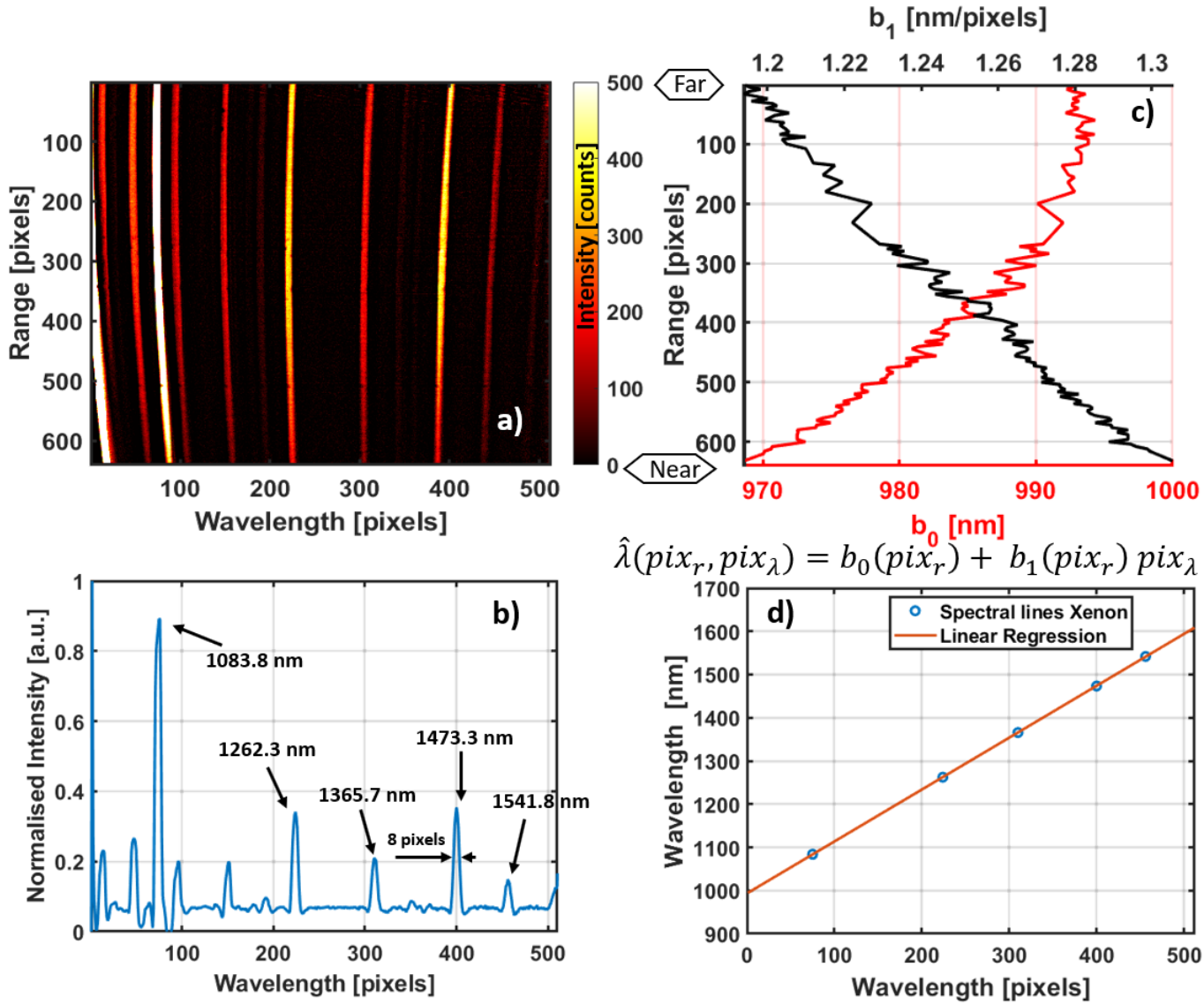

Figure 25: Spectral calibration using a Xenon-lamp. a) Spectral emission lines of Xe recorded with EHSL 2.0. b) Spectrum in the far range with the assigned values in nm. d) Linear regression to convert the pixel values to wavelengths in nm. c) Parameters of linear regression as a function of range.

The spectral sensitivity of the EHSL 2.0 (fig. 26) is comparable to the one in EHSL 1.0 (fig 21). The spectral range for the EHSL 2.0 is slightly decreased, owing the choice of lenses and grating.

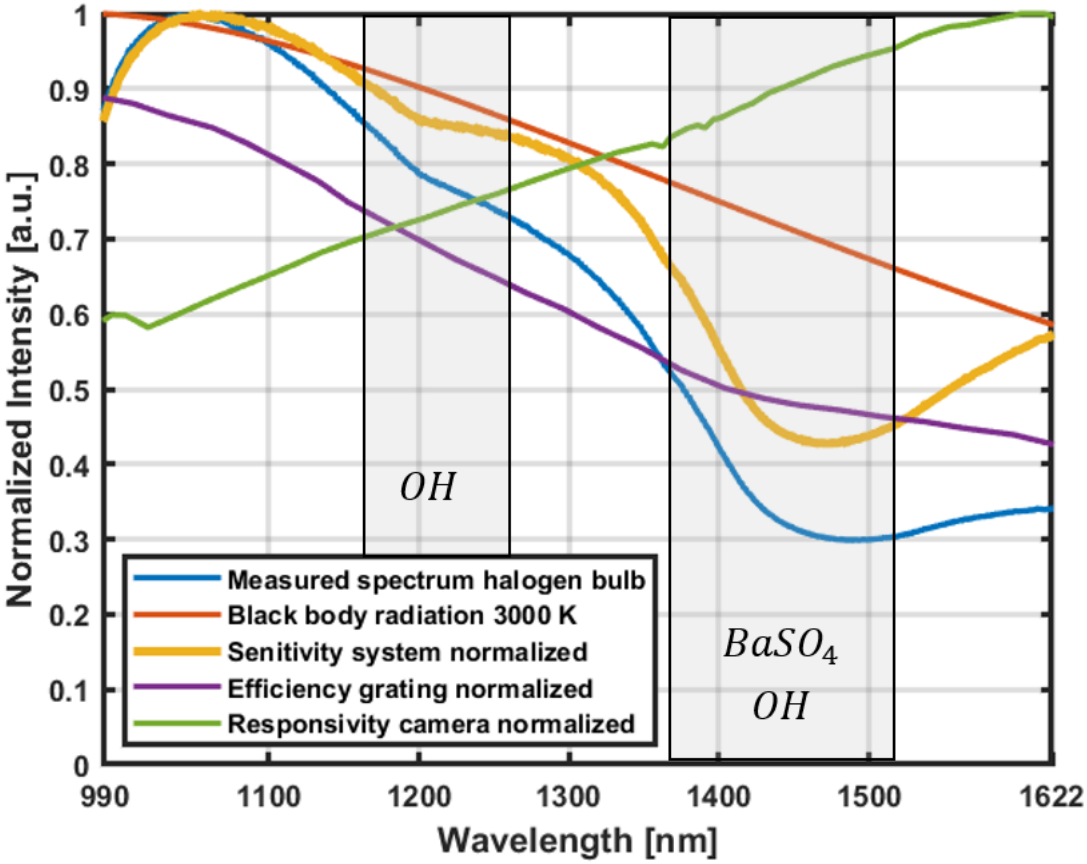

Figure 26: Spectral sensitivity plot of the EHSL 2.0 (orange), using the measured blackbody radiation of a halogen bulb (3000 K) (blue) which is compared to the theoretical black-body radiation at 3000 K (red). The grating efficiency (purple) and the camera responsivity (green) are plotted as well. The dips appearing in the sensitivity plot at ≈ 1200 nm and ≈ 1400 nm are caused by the BaSO4 coating of the integrating sphere and by OH from the quartz glass of the halogen bulb, respectively.

As for the EHSL 1.0 in figure 22 a), the spectral sensitivity for the EHSL 2.0 was plotted at three different range positions (see fig. 27 a)). From figure 27 b) it is evident that now the entire sensor is illuminated. The flat-field in figure 27 c) is approaching a top-hat profile as opposed to flat-field of the EHSL 1.0 (see fig. 22 c)). The drop in intensity at far and near might be caused by the illumination rather than the performance of the system, as the illumination did not reach the far and near end of the slit as good as the center. The illumination exiting from the outlet of the integrating sphere is placed in front of the slit according to figure 18.

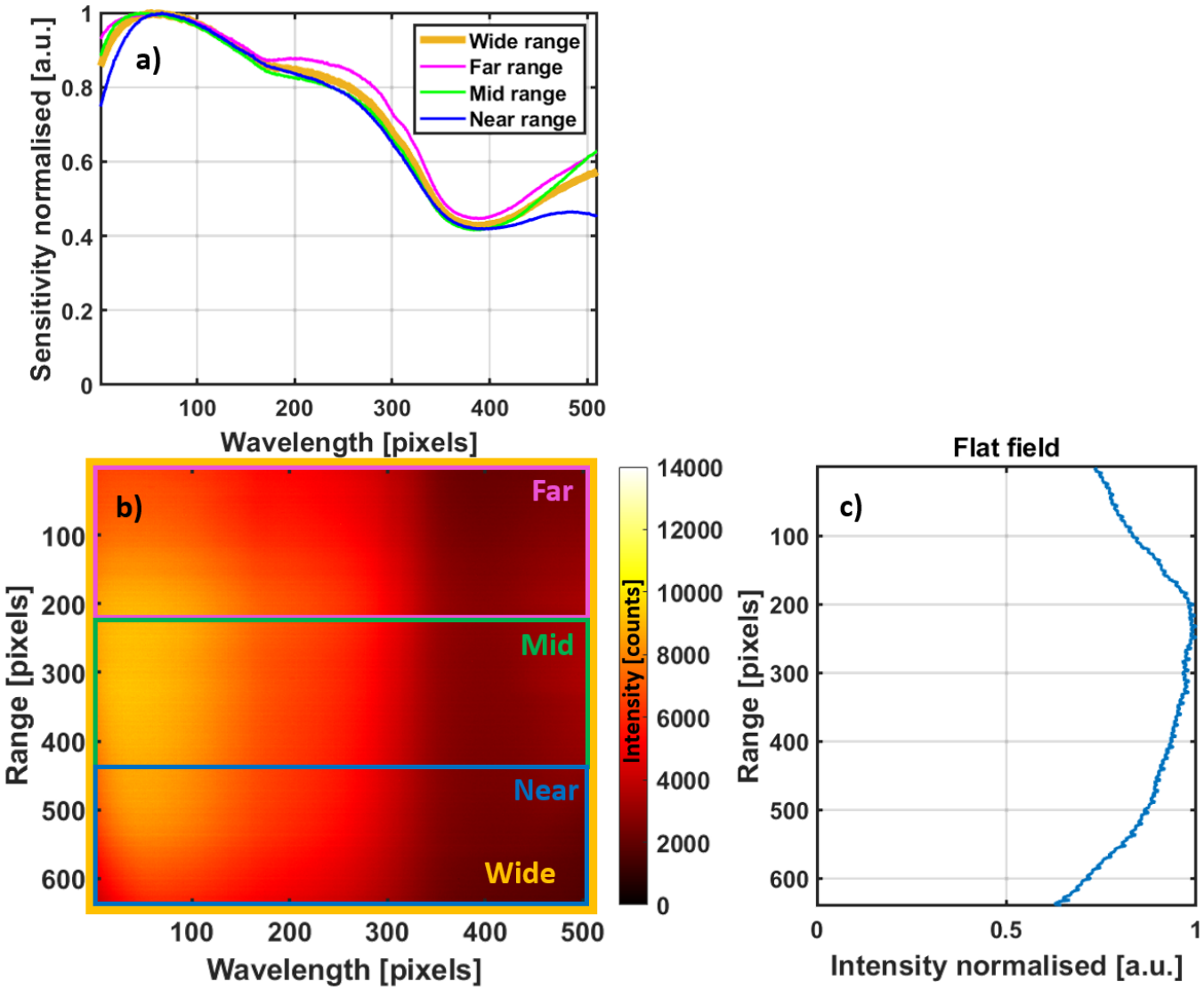

Figure 27: a) Spectral sensitivity plot of the EHSL 2.0, at three different range positions using the blackbody radiation of a halogen bulb. b) Detector-image with uniformly illuminated slit. c) Flat-field which is the intensity as a function of range. For a uniform illumination, the flat-field is expected to feature a top-hat profile.

6 EHSL field measurements

Evenetually, the spectral analyser was tested during a field campaign at Stensoffas field station in southern Sweden. The lidar was placed on a tripod and protected by a car port tent. A neoprene termination was placed 100 m away. The purpose of the termination is on the one hand to terminate the beam and on the other hand to have a reference which later will be used for range and spectral calibration. The lidar is set up similar to what is discussed in chapter 3. A monitor camera is utilized to keep track of the laser spot which is invisible for the human eye. Figure 28 shows the setup of the lidar during the field measurements.

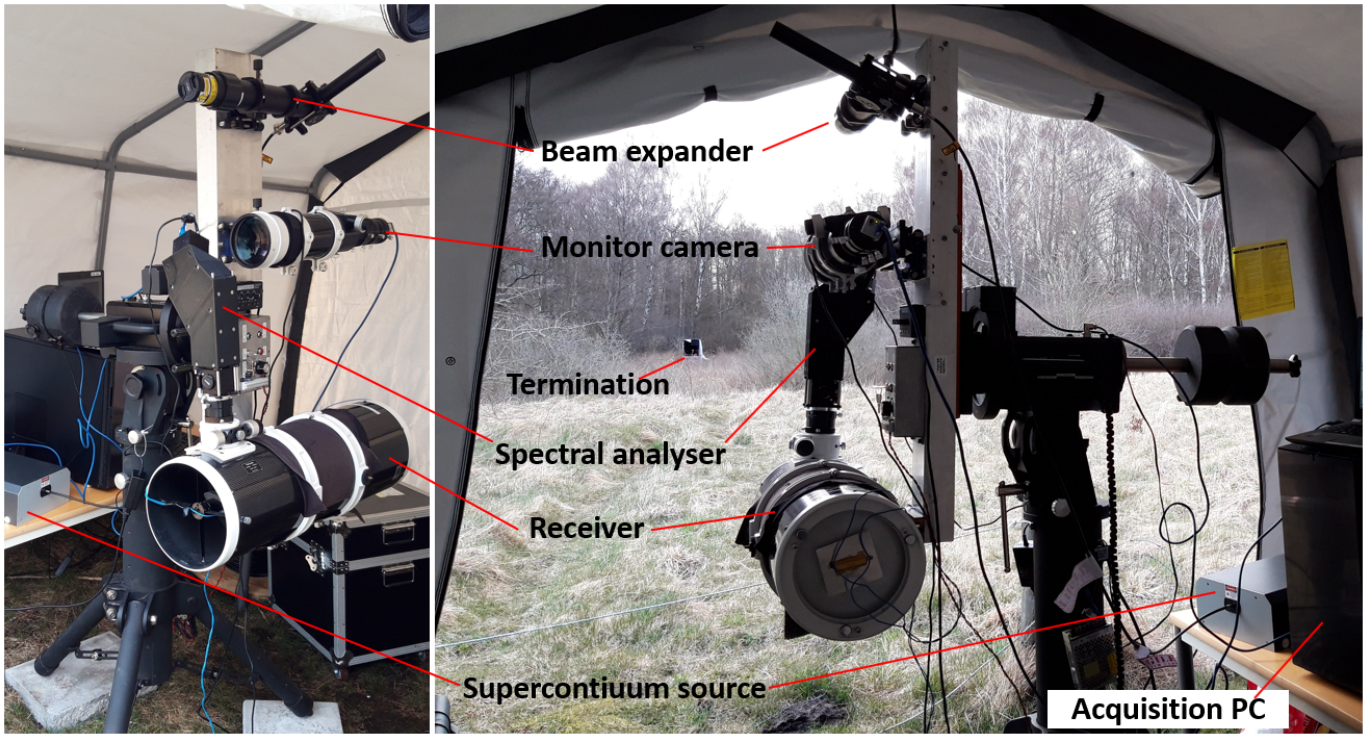

Figure 28: Fully mounted EHSL pointing at the termination during field measurements at Stensoffas field station.

The measurements were conducted during the night to reduce background illumination. Modulating the source is not possible at the moment which would allow continuous background subtraction. Figure 29 shows the supercontinuum laser beam emerging from the lidar and pointing at the termination.

Figure 29: EHSL during field measurement at Stensoffas field station with the super continuum laser beam pointing at the termination.

Different wings from museum specimen of dragonflies and damselflies were held into the beam at 87 m away from the lidar. As a proof of principle the coherent backscatter from the wings was measured. The wings from dragonflies and damselflies are made of chitin and can be approximated as a thin film membrane. Hence, the specular reflections may result in interference fringe pattern as discussed in chapter 2.2. From the thin-film pattern, the wing thickness can be determined.

The images from the camera of the spectral analyser were acquired with a Labview program which generated the hyperspectral datacube (see chapter 3.6) by stacking a sequence of exposures and saving them on a external harddrive as raw files. The images were acquired with an exposure time of 4 ms and a framerate of 200 Hz.

7 Data analysis

7.1 Range-time map

The data recorded during the field measurements (see chapter 6) was analysed in Matlab. With 200 images per second, a significant amount of data has to be analysed to retrieve the few exposures with a relevant signal. In figure 30 a range-time map is plotted to locate the files of interest. The recorded datacubes consist of 200 exposures. The dimension of each data cube was reduced by taking the median of the different exposures as well as the median of the spectrum, resulting in a 1D-vector with a median intensity value at each range position. The range conversion from pixels to meters is done with a Matlab script which was available from previous lidar measurements of the research group. A detailed explanation of the conversion is found in [31].
With the approximate time when the different samples were measured, the samples could be allocated to the files.

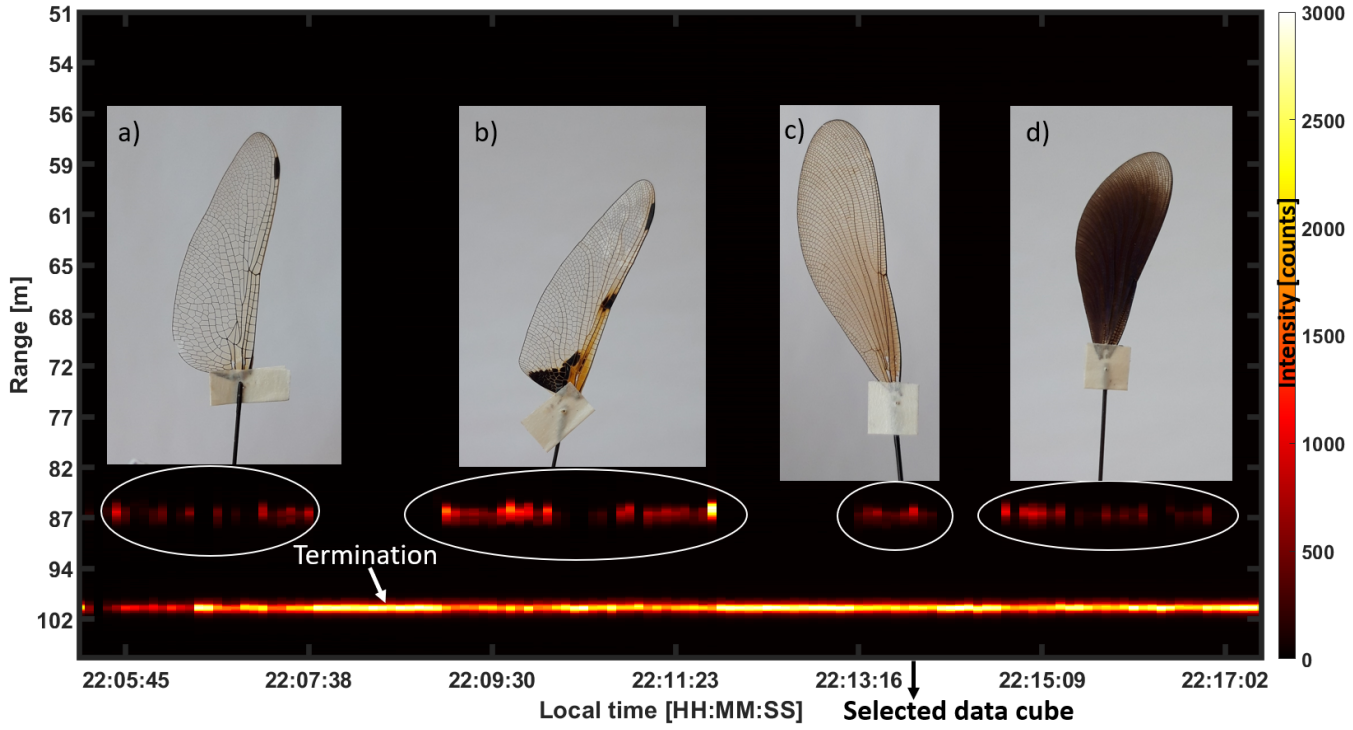

Figure 30: Range-time map with the signals of four different samples. a) Dragonlfy, *Orthetrum Cancellatum*, b) Dragonfly, *Libellula quadrimaculata*, c) Damselfly, *Calopteryx Virgo*, female, d) Damselfly, *Calopteryx Virgo*, male

7.2 Fringe damselfly

In this thesis the thin-film fringe of the female damselfly (fig. 30 c)) was analysed in detail. The selected data cube is indicated in figure 30. One data cube consists of 200 exposures.

A background file was recorded at the beginning of the measurement by blocking the light of the source.
Each exposure of a data cube was then subtracted by the same background file before proceeding with the data analysis. The background subtraction addresses problems such as pixel specific gain and dark current. The picture of a single exposure is depicted in figure 31 a) with the dimensions of the detector being range and wavelength. The picture reveals the spectrum of the termination and sample, respectively. The enhanced signal at 1064 nm is from the Nd:YAG pump laser (see spectrum in fig. 9).
In figure 31 b), the measured intensity is plotted as a function of range for three different wavelengths using the same exposure as in figure 31 a).
Figure 31 c) shows the spectra in reflectance for each of the 200 exposures in the selected data cube.
The reflectance R is the total backscattered light effected by the sample and is calculated as,

$$R = R_{\text{term}} \cdot \frac{I_{r_{\text{sample}},\,\lambda,\,t_{\text{sample}}} \cdot r^2_{\text{sample}}}{I_{r_{\text{term}},\,\lambda,\,t_{\text{sample}}} \cdot r^2_{\text{term}} \cdot \eta}, \tag{9}$$

where I is the intensity with the subscript indicating where in the hyperspectral data cube (see fig. 11) the range, wavelength and time, is measured. r_{sample} and r_{term} are the range positions of the sample and the termination, respectively. t_{sample} is the time, the sample was measured. For instance, $I_{r_{\text{sample}},\,\lambda,\,t_{\text{sample}}}$ is the measured intensity at the range position and time of the sample for all wavelengths.
R_{term} is the reflectance of the neoprene termination and is $R_{\text{term}} = 2\,\%$ across the visible, near infrared and SWIR range and was measured with a hyperspectral camera (Hyspex, Norsk Elektro Optikk, Norway). η describes the fraction of light, hitting the sample and is defined as,

$$\eta = 1 - \frac{I_{r_{\text{term}},\,\lambda,\,t_{\text{sample}}}}{I_{r_{\text{term}},\,\lambda,\,t_{\text{static}}}}, \tag{10}$$

where $I_{r_{\text{term}},\,\lambda,\,t_{\text{sample}}}$ is the intensity of the termination with a sample in front of it and $I_{r_{\text{term}},\,\lambda,\,t_{\text{static}}}$ the intensity of the termination when no sample is shielding part of the light.
Figure 31 c) reveals spectra with high and low intensities. These features are caused by structural colors, namely thin-film interference. The maxima and minima are shifting in time, as the surface normal orientation was varied during the measurement. Spectral features such as fringes of a thin-film membrane shift towards shorter wavelength when incident and observation angles are increased from surface normal (see eq. 6.39 in [2]).
The reflectance spectrum of the damselfly wing is plotted in figure 31 d) and reveals a thin-film fringe pattern. The same single exposure was used for figure 31 a),b) and d). The thin-film interference model R_{thinfilm} from equation 2 was multiplied with a long pass function to match the low reflectance at short wavelengths. The complete reflectance model R_{wing} which was used to fit the data is,

$$R_{\text{wing}} = \frac{\left(\frac{\lambda}{\lambda_0}\right)^{\alpha}}{1+\left(\frac{\lambda}{\lambda_0}\right)^{\alpha}} \cdot \left(R_{\text{long}} + R_{\text{fringe}} \cdot \frac{4R_{\text{Fresnel}}^2 \sin^2(2\pi d\sqrt{n_{\text{chitin}}^2 - \sin^2\theta}/\lambda)}{(1-R_{\text{Fresnel}}^2)^2 + 4R_{\text{Fresnel}}^2 \sin^2(2\pi d\sqrt{n_{\text{chitin}}^2 - \sin^2\theta}/\lambda)} \right), \tag{11}$$

where the wing thickness d is to be determined and λ_0, R_{long}, R_{fringe} and α are parameters of the fitting-model. R_{Fresnel} is the reflectance from the Fresnel equations, θ the angle of incidence and n_{chitin} the refractice index of chitin. R_{Fresnel}, θ and n_{chitin} are defined with the thin-film model R_{thinfilm} in equation 2.
The resulting parameters from the fitting-model are listed in table 1 with a confidence interval of 95 % and $R_{\text{adj}}^2 = 96\,\%$.

Table 1: Parameters from fitting-model in equation 11 with a confidence interval of 95 % and $R_{\text{adj}}^2 = 96\,\%$.

Parameter	Value	Confidence interval 95 %	Unit
d	1417	$(1414, 1421)$	nm
λ_0	1398	$(1361, 1436)$	nm
R_{long}	12.95	$(11.51, 14.4)$	%
R_{fringe}	107.5	$(97.99, 117)$	%
α	8.359	$(7.632, 9.086)$	

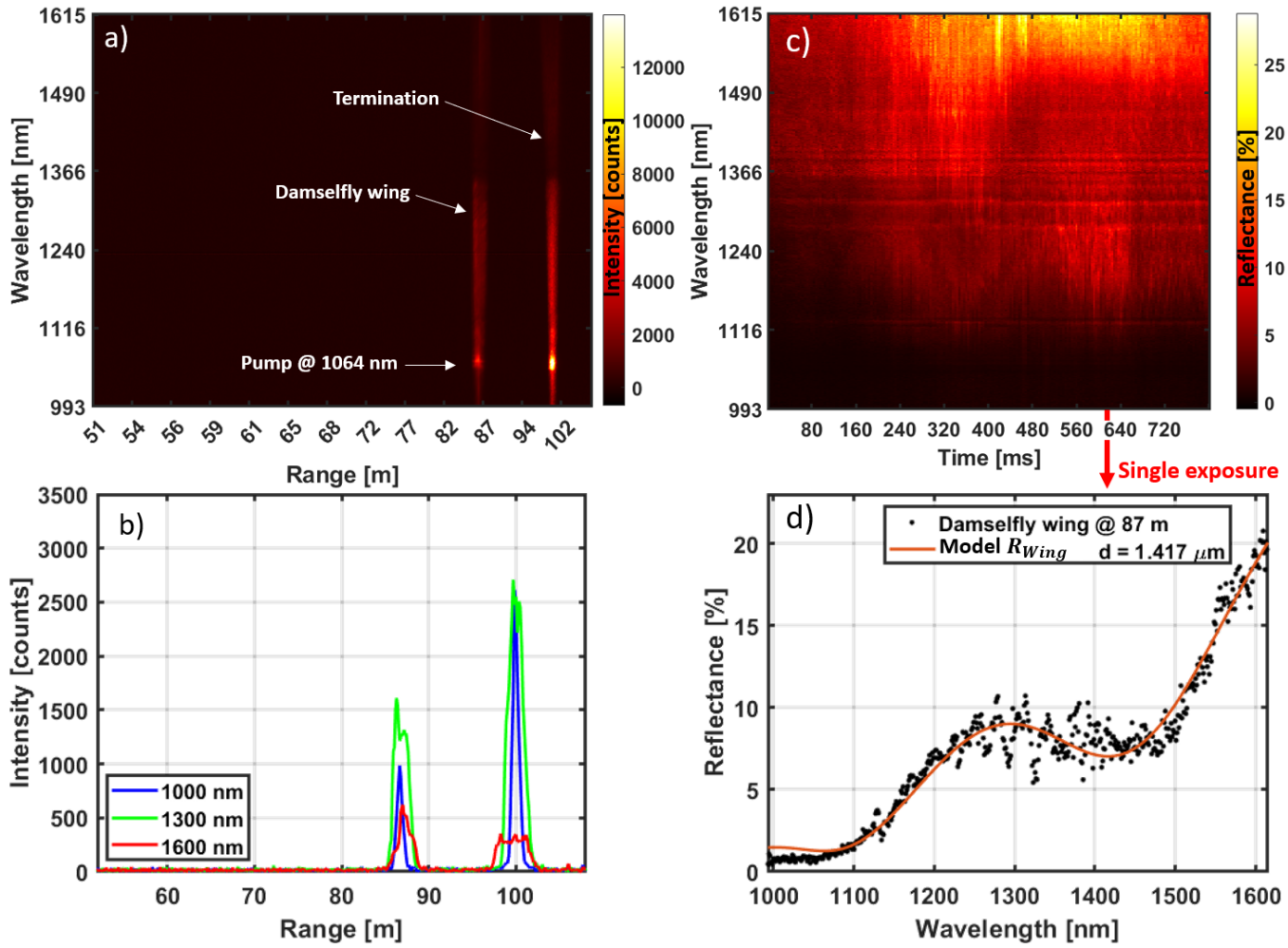

Figure 31: a) Single exposure (4 ms) of damselfly wing measured at 87 m showing the spectrum and range of the sample and the termination, respectively. b) Intensity-range map for three different wavelengths using the same exposure as in a). c) Reflectance spectra for each of the 200 exposures in a datacube. The reflectance spectrum of a single exposure is plotted in panel d) featuring a thin-film interference pattern from which the wing thickness can be determined. Note that the single exposure which is indicated in panel c), was used for a),b) and d).

7.3 Comparing with reference measurement

In order to compare the obtained result of the wing thickness $d = 1417\,\text{nm}$, the same damselfly wing was measured with a commercial hyperspectral camera (Hyspex, Norsk Elektro Optikk, Norway). The result is presented in figure 32. Figure 32 a) is a photo of the damselfly wing and figure 32 b) a color coded figure of the same wing illustrating the thickness at each position of the wing. It becomes obvious that the thickness varies significantly over the entire wing. A histogram of the appearing thicknesses is found in figure 32 c). An average fringe of the entire wing is depicted in figure 32 d). The measurement with the Hyspex camera was conducted at an angle of 56 °, while the angle in the field measurements was $\approx 0\,°$. Spectral

features, i.e. fringes of thin-film membranes, shift towards shorter wavelength when incident and observation angles are increased from surface normal. This has to be considered when comparing the fringe pattern from the lidar measurement in figure 31 d) with the reference measurement in figure 32 d).

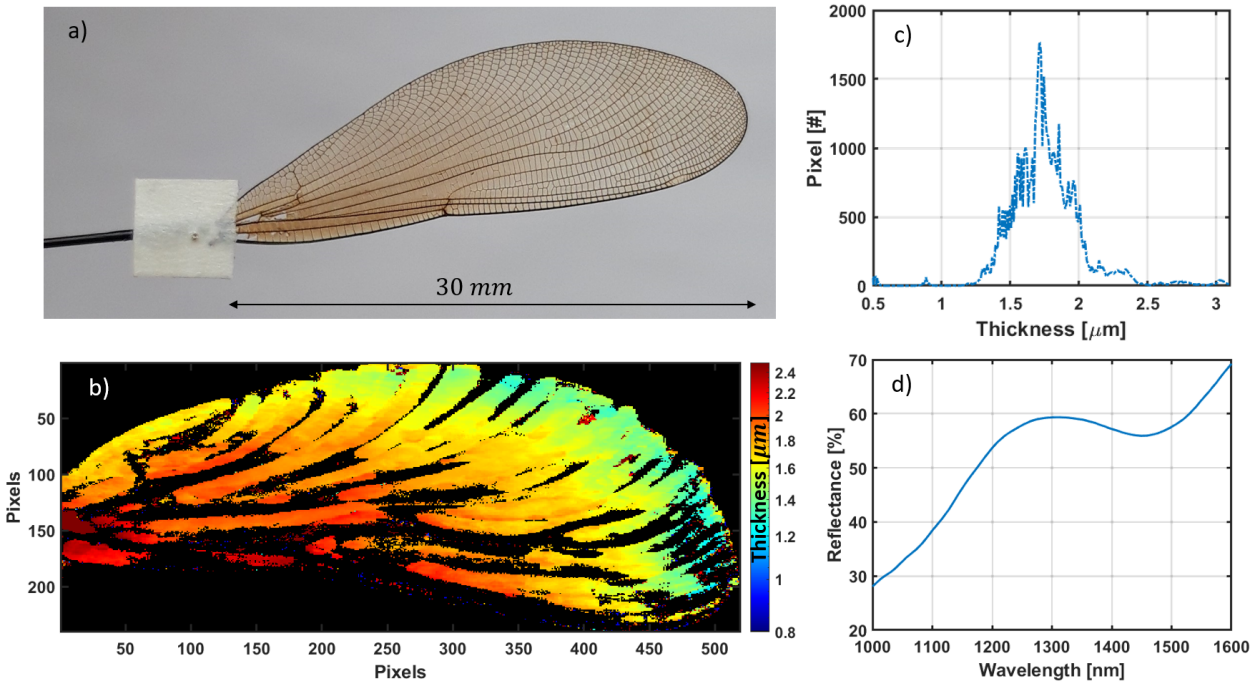

Figure 32: Lab measurements to compare the obtained result with. a) Photo of damselfly wing which was used during field measurements. b) Color-coded image showing the wing thickness, determined from lab measurements with a commercial hyperspectral camera, (Hyspex, Norsk Elektro Optikk). c) Histogram with the occurring thicknesses and d) an averaged fringe of the entire wing. Credit: Meng Li

8 Discussion

Despite the relatively broad spectral range of $\Delta\lambda \approx 620\,\text{nm}$, the spectral analyser was designed with lenses instead of mirrors. Mirrors do not cause chromatic aberrations which is beneficial when working with an increased spectral range. However, the relatively short focal length of the focusing lens that was required to achieve the spectral range $\Delta\lambda$ (see chapter 4.1) would have had the consequence of the detector being to close to the mirror and blocking the incoming light. The optical system could be further improved by using best form lenses instead of spherical lenses which would reduce the spherical aberrations. Moreover, adding a negative lens to the focusing lens unit would act a field-flattener lens and reduce field curvature. The use of smaller optics would cut-off rays from the far and near range resulting in a more pyramid-shape flat-field (fig. 27c)). However, the optical performance

in terms of spot-size would be increased, as spherical aberrations mainly are caused by the rays far from the optical axis.

During the characterisation which is discussed in chapter 5, the available integrating sphere had a working range only up to $\approx 1200\,\text{nm}$ which caused absorption dips in the illumination. In order to achieve a more representative calibration result, an integrating sphere designed for the SWIR regime should be used.

The result obtained for the damselfly wing $d = 1417\,\text{nm}$ is for a particular area of the wing whose specular reflection was collected with the receiver telescope. It is unknown from what part of the wing the reflection arose and how many wing cells contributed to the fringe. The obtained result is in good agreement with the lab measurement in figure 32. The histogram in figure 32 c) as well as the color coded image in figure 32 b) state that the wing exhibits a significant amount of areas with the thickness $d = 1.4\,\mu\text{m}$.

It is evident that the fringe measured with the lidar (fig. 31 d)) and the one with the commercial hyperspectral camera (fig. 32 d) decrease in amplitude at shorter wavelengths. According to the thin-film model in equation 2, however, interference fringes exhibit a constant amplitude. Several effects might have contributed to the decrease in amplitude at shorter wavelengths.
The surface of damselflies can exhibit small protrusions which create a gradient refractive index at the boundary from air to chitin, as opposed to a refractive index step function. Such a gradient refractive index acts as a anti-reflection layer [14] which is more effective for shorter wavelengths, as the gradient along the propagation of light occupies a larger fraction of the wavelength. From an evolutionary point of view, the damselfly developed this anti-reflection layer to not be seen by predators, mainly birds, with vision in the visible regime.
Another reason for the attenuated reflectance for shorter wavelengths might be the faint amount of melanin which is contained in the chitin of the wing. Melanin absorbs more light at shorter wavelengths and might therefore reduce the reflectance at $\approx 1000\,\text{nm}$.
The determined wing thickness $d = 1417\,\text{nm}$ is calculated with the refractive index of chitin which is $n_{\text{chitin}} = 1.522$ at $1300\,\text{nm}$. The presence of melanin would change the refractive index slightly and induce an error in the determined geometrical thickness.

9 Conclusion and outlook

The spectral analyser designed in this thesis has 64 effective spectral bands in the SWIR-range which to our knowledge, currently no other full-waveform lidar exhibits. This lidar could bring the specificity for in-situ insect surveillance to a new level. As discussed in chapter 1.1, this device could furthermore be used to determine the surface roughness of moth and also for measuring the equivalent path length of melanin and water.

Typical wing beat frequencies of insects span from 10 Hz − 1000 Hz. With a frame rate of 600 Hz of the InGaAs camera, wing beat frequencies could theoretically be resolved, especially for 'low frequency insects' such as dragonflies, damselflies and moth. The wing beat frequency of dragonflies, for instance, is at 50 Hz. With a frame rate of 600 Hz, it could not be excluded that multiple fringes are recorded during one wing beat.
The result obtained for the damselfly wing, $d = 1417$ nm, is given within an excellent precision of ± 4 nm. While this result is obtained by holding a wing of a museum specimen into the beam, additional difficulties have to be faced when measuring flying insects. For instance, not only the wing but the entire body might contribute to the signal and result in a less distinct interference pattern. Luckily, the signal of body and wing can be separated as they exhibit different frequency components. While the wing of a dragonfly is flapping at 50 Hz, the body signal can be considered as the DC-component. Moreover, in order to collect the specular reflection with the receiver, the incident angle needs to be around 0 °, depending on the flight direction of the insect, this might not always be the case and only diffuse reflection is collected. Finally, the system is requiring low background illumination and is thus not working at daylight. Dragonflies and damselflies, however, do not fly at night. Being able to modulate the laser source would allow background subtraction of each exposure and possibly solve this issue. However, we are currently not able to modulate the supercontiuum light source. Nevertheless, measuring the thickness of a damselfly wing at a distance of 87 m with a precision of ± 4 nm is a very promising result for future entomological studies and can bring species specificity of remote sensing of insects to a new level.

During the field campaign in April 2022 at Stensoffas fieldstation, not only dragonlfies and damselflies but also other samples were measured such as moth, gases and different powders. So far only the data for the damselfly was analysed. Analysing the additional data might result in additional results. As a next step, the system has to be tested on free flying insects.

10 Related work

During a field campaign in August 2021 at Stensoffas field station, different measurements with a similar, inelastic hyperspectral lidar were conducted. The lidar used a laser at 405 nm to induce fluorescent emission which was measured from different samples. In figure 33, a mosquito which was fed with a fluorescent sugar solution is depicted. The fluorescent emission could be measured on free-flying individuals. In addition to mosquitoes, the fluorescent emission from powdered honey bees could be measured at daylight. The field campaign resulted in an article, see [27].

Figure 33: Mosquito fed with a fluorescent sugar solution. Here, the fluorescence is induced with a torch in the ultra-violet.

Moreover, the same inelastic lidar was used to scan a forest with different types of vegetation. Figure 34 shows a long exposure image (30 s) revealing the laser beam at 405 nm that scans a forest area of $\approx 50\,\mathrm{m} \times 10\,\mathrm{m}$. The fluorescent emission of the chlorophyll could be detected which will be used as a fingerprint to discriminate different types of vegetation.

Figure 34: Inelastic hyperspectral lidar using a laser beam at 405 nm which scans a forest area and measures the induced fluorescent emission of the chlorophyll.

References

[1] VA K, WE E. Elastic lidar : theory, practice, and analysis methods. Wiley Interscience; 2004.

[2] Svanberg S. Atomic and molecular spectroscopy: basic aspects and practical applications. vol. 6. Springer Science & Business Media; 2012.

[3] Larsson J, Bood J, Xu CT, Yang X, Lindberg R, Laurell F, et al. Atmospheric CO 2 sensing using Scheimpflug-lidar based on a 1.57-μm fiber source. Optics Express. 2019;27(12):17348-58.

[4] Zhao G, Malmqvist E, Török S, Bengtsson PE, Svanberg S, Bood J, et al. Particle profiling and classification by a dual-band continuous-wave lidar system. Applied Optics. 2018;57(35):10164-71.

[5] Brydegaard M, Larsson J, Török S, Malmqvist E, Zhao G, Jansson S, et al. Short-wave infrared atmospheric Scheimpflug lidar. In: EPJ Web of Conferences. vol. 176. EDP Sciences; 2018. p. 01012.

[6] Zhao G, Ljungholm M, Malmqvist E, Bianco G, Hansson LA, Svanberg S, et al. Inelastic hyperspectral lidar for profiling aquatic ecosystems. Laser & Photonics Reviews. 2016;10(5):807-13.

[7] Wang X, Duan Z, Brydegaard M, Svanberg S, Zhao G. Drone-based area scanning of vegetation fluorescence height profiles using a miniaturized hyperspectral lidar system. Applied Physics B. 2018;124(11):1-5.

[8] Brydegaard M, Svanberg S. Photonic monitoring of atmospheric and aquatic fauna. Laser & Photonics Reviews. 2018;12(12):1800135.

[9] Hallmann CA, Sorg M, Jongejans E, Siepel H, Hofland N, Schwan H, et al. More than 75 percent decline over 27 years in total flying insect biomass in protected areas. PloS one. 2017;12(10):e0185809.

[10] Seibold S, Gossner MM, Simons NK, Blüthgen N, Müller J, Ambarlı D, et al. Arthropod decline in grasslands and forests is associated with landscape-level drivers. Nature. 2019;574(7780):671-4.

[11] Brydegaard M. Advantages of shortwave infrared LIDAR entomology. In: Imaging and Applied Optics 2014. Optica Publishing Group; 2014. p. LW2D.6. Available from: `http://opg.optica.org/abstract.cfm?URI=LACSEA-2014-LW2D.6`.

[12] Brydegaard M, Jansson S, Schulz M, Runemark A. Can the narrow red bands of dragonflies be used to perceive wing interference patterns? Ecology and evolution. 2018;8(11):5369-84.

[13] Li M, Jansson S, Runemark A, Peterson J, Kirkeby CT, Jönsson AM, et al. Bark beetles as lidar targets and prospects of photonic surveillance. Journal of Biophotonics. 2021;14(4):e202000420.

[14] Stavenga DG. Thin film and multilayer optics cause structural colors of many insects and birds. Materials Today: Proceedings. 2014;1:109-21.

[15] Tay C, Wang S, Quan C, Shang H. In situ surface roughness measurement using a laser scattering method. Optics Communications. 2003;218(1-3):1-10.

[16] Basistyy R, Genoud A, Thomas B. Backscattering properties of topographic targets in the visible, shortwave infrared, and mid-infrared spectral ranges for hard-target lidars. Applied Optics. 2018;57(24):6990-7.

[17] Li M, et al. Identification of wild night-flying moths by remote infrared microscopy.

[18] Mei L, Brydegaard M. Continuous-wave differential absorption lidar. Laser & Photonics Reviews. 2015;9(6):629-36.

[19] Shoshanim O, Baratz A. Daytime measurements of bioaerosol simulants using a hyperspectral laser-induced fluorescence LIDAR for biosphere research. Journal of Environmental Chemical Engineering. 2020;8(5):104392.

[20] Hakala T, Suomalainen J, Kaasalainen S, Chen Y. Full waveform hyperspectral LiDAR for terrestrial laser scanning. Opt Express. 2012 Mar;20(7):7119-27. Available from: http://opg.optica.org/oe/abstract.cfm?URI=oe-20-7-7119.

[21] Malkamäki T, Kaasalainen S, Ilinca J. Portable hyperspectral lidar utilizing 5 GHz multichannel full waveform digitization. Opt Express. 2019 Apr;27(8):A468-80. Available from: http://opg.optica.org/oe/abstract.cfm?URI=oe-27-8-A468.

[22] Brydegaard M, Malmqvist E, Jansson S, Larsson J, Török S, Zhao G. The Scheimpflug lidar method. In: Lidar Remote Sensing for Environmental Monitoring 2017. vol. 10406. SPIE; 2017. p. 104-20.

[23] Malmqvist E, Brydegaard M, Aldén M, Bood J. Scheimpflug lidar for combustion diagnostics. Optics express. 2018;26(12):14842-58.

[24] Liu Z, Li L, Li H, Mei L. Preliminary studies on atmospheric monitoring by employing a portable unmanned Mie-scattering Scheimpflug lidar system. Remote Sensing. 2019;11(7):837.

[25] Li W, Sun G, Niu Z, Gao S, Qiao H. Estimation of leaf biochemical content using a novel hyperspectral full-waveform LiDAR system. Remote sensing letters. 2014;5(8):693-702.

[26] Du L, Gong W, Shi S, Yang J, Sun J, Zhu B, et al. Estimation of rice leaf nitrogen contents based on hyperspectral LIDAR. International Journal of Applied Earth Observation and Geoinformation. 2016;44:136-43.

[27] Månefjord H, Müller L, Li M, Salvador J, Blomqvist S, Runemark A, et al. 3D-Printed Fluorescence Hyperspectral Lidar for Monitoring Tagged Insects. IEEE Journal of Selected Topics in Quantum Electronics. 2022;28(5):1-9.

[28] Zhao G, Malmqvist E, Rydhmer K, Strand A, Bianco G, Hansson LA, et al. Inelastic hyperspectral lidar for aquatic ecosystems monitoring and landscape plant scanning test. In: EPJ Web of Conferences. vol. 176. EDP Sciences; 2018. p. 01003.

[29] Eckbreth AC. Laser diagnostics for combustion temperature and species. vol. 3. CRC press; 1996.

[30] Saleh BE, Teich MC. Fundamentals of photonics. john Wiley & sons; 2019.

[31] Malmqvist E. From Fauna to Flames : Remote Sensing with Scheimpflug Lidar. Lund University; 2019. Available from: `https://lup.lub.lu.se/search/files/60914506/Fauna_to_Flames.pdf`.

[32] Boudoux C. Fundamentals of Biomedical Optics: From Light Interaction with Atoms and Molecules to Complex Imaging Systems. Pollux; 2016.

[33] Yin H, Shi L, Sha J, Li Y, Qin Y, Dong B, et al. Iridescence in the neck feathers of domestic pigeons. Physical Review E. 2006;74(5):051916.

[34] Engström J, Nygren J, Aldén M, Kaminski C. Two-line atomic fluorescence as a temperature probe for highly sooting flames. Optics Letters. 2000;25(19):1469-71.

[35] Carpentier J. Improvements in enlarging or like cameras. Great Britain Patent. 1901;1139.

[36] Scheimpflug T. Improved method and apparatus for the systematic alteration or distortion of plane pictures and images by means of lenses and mirrors for photography and for other purposes. GB patent. 1904;1196.

[37] MAYER H. SCHEIMPFLUG, THEODOR-HIS PERSONALITY AND LIFEWORK. KARGER ALLSCHWILERSTRASSE 10, CH-4009 BASEL, SWITZERLAND; 1994.

[38] Mei L, Brydegaard M. Atmospheric aerosol monitoring by an elastic Scheimpflug lidar system. Optics Express. 2015;23(24):A1613-28.

[39] Ljungholm M. Inelastic lidar for monitoring aquatic fauna. 2016.

[40] Photonics N. Supercontinuum generation in photonics crystal fibers. NKT Photonics–Blokken. 2009;84:3460.

[41] Sze SM, Lee MK. Semiconductor devices : physics and technology. Wiley-Blackwell; 2012.

[42] James J. Spectrograph design fundamentals. Cambridge University Press; 2007.

[43] Martin L. How to build a spectrometer;. Available from: `https://support.zemax.com/hc/en-us/articles/1500005578862`.

[44] Hobbs PCD. Building electro-optical systems : making it all work. Wiley series in pure and applied optics. Wiley; 2000. Available from: http://ludwig.lub.lu.se/login?url=https://search.ebscohost.com/login.aspx?direct=true&db=cat07147a&AN=lub.1534674&site=eds-live&scope=site.

[45] Aikio M. Hyperspectral prism-grating-prism imaging spectrograph: Dissertation. Finland: University of Oulu; 2001.

[46] Høye G, Løke T, Fridman A. Method for quantifying image quality in push-broom hyperspectral cameras. Optical Engineering. 2015;54(5):053102.

[47] Høye G, Fridman A. Mixel camera—-a new push-broom camera concept for high spatial resolution keystone-free hyperspectral imaging. Opt Express. 2013 May;21(9):11057-77. Available from: http://opg.optica.org/oe/abstract.cfm?URI=oe-21-9-11057.

[48] Kristensson E, Bood J, Alden M, Nordström E, Zhu J, Huldt S, et al. Stray light suppression in spectroscopy using periodic shadowing. Opt Express. 2014 Apr;22(7):7711-21. Available from: http://opg.optica.org/oe/abstract.cfm?URI=oe-22-7-7711.